Investigating the spectral age problem with powerful radio galaxies

Vijay H. Mahatma [,1]* Martin J. Hardcastle [,1] Judith H. Croston,[2]
Jeremy Harwood [,1] Judith Ineson[3] and Javier Moldon[4,5]

[1]*Centre for Astrophysics Research, School of Physics, Astronomy & Mathematics, University of Hertfordshire, College Lane, Hatfield AL10 9AB, UK*
[2]*School of Physical Sciences, The Open University, Walton Hall, Milton Keynes MK7 6AA, UK*
[3]*School of Physics and Astronomy, University of Southampton, Southampton S17 1BJ, UK*
[4]*Jodrell Bank Centre for Astrophysics, School of Physics and Astronomy, University of Manchester, Manchester M13 9PL, UK*
[5]*Instituto de Astrofísica de Andalucía (IAA, CSIC), Glorieta de las Astronomía, s/n, E-18008 Granada, Spain*

ABSTRACT

The 'spectral age problem' is our systematic inability to reconcile the maximum cooling time of radiating electrons in the lobes of a radio galaxy with its age as modelled by the dynamical evolution of the lobes. While there are known uncertainties in the models that produce both age estimates, 'spectral' ages are commonly underestimated relative to dynamical ages, consequently leading to unreliable estimates of the time-averaged kinetic feedback of a powerful radio galaxy. In this work, we attempt to solve the spectral age problem by observing two cluster-centre powerful radio galaxies; 3C 320 and 3C 444. With high-resolution broadband Karl G. Jansky Very Large Array observations of the radio sources and deep *XMM–Newton* and *Chandra* observations of their hot intracluster media, coupled with the use of an analytic model, we robustly determine their spectral and dynamical ages. After finding self-consistent dynamical models that agree with our observational constraints, and accounting for sub-equipartition magnetic fields, we find that our spectral ages are still underestimated by a factor of two at least. Equipartition magnetic fields will underestimate the spectral age by factors of up to $\sim$20. The turbulent mixing of electron populations in the radio lobes is likely to be the main remaining factor in the spectral age/dynamical age discrepancy, and must be accounted for in the study of large samples of powerful radio galaxies.

Key words: radiation mechanisms: non-thermal – shock waves – methods: observational – galaxies: active – galaxies: clusters: intracluster medium – galaxies: jets.

1 INTRODUCTION

1.1 Radio galaxies and their environments

Radio galaxies, or radio-loud active galactic nuclei (RLAGN), drive powerful jets of plasma into the environment of their host galaxies, inflating large radio-emitting lobes seen in radio observations. It is now well known that such large-scale radio emission (physical linear scales of a few Mpc for the largest sources, e.g. Dabhade et al. 2017) originates from the process of accretion on to the supermassive black hole (SMBH) of the host galaxy, where the jets are launched. For the most powerful sources, which tend to be hosted by massive elliptical galaxies (Best 2004; Best & Heckman 2012; Sabater et al. 2019), the jets may escape their central dense environments and terminate in the intergalactic (IGM) or intracluster medium (ICM).

The jets of RLAGN can have profound implications for cosmic evolution. The widely postulated AGN feedback mechanism (e.g.

Croton et al. 2006; Wylezalek & Zakamska 2016) attempts to account for the shape of the galaxy mass function, which shows a steep decline of galaxies with increasing stellar mass. One of the mechanisms by which this can physically be explained is interstellar gas heating by the jets, which is suggested to be linked to the suppression of star formation in the most massive galaxies. While as yet there is no direct observational evidence for the population of RLAGN in general affecting their host-galaxy star-formation rates, there *is* robust evidence for significant heating of the interstellar or intracluster gas by powerful jets as they drive shocks into their surrounding medium (e.g. Kraft et al. 2003; Croston, Kraft & Hardcastle 2007; Croston et al. 2009; Liu et al. 2019). To understand what role this heating plays in the evolution of galaxies or clusters, it is important to understand and quantify the energetics of AGN during a radio-loud jet outburst, and how long they spend in this phase.

Of particular importance is the power output of a radio galaxy during each outburst (the jet power), which is a useful quantity for models of feedback processes (Heinz et al. 2007; Gaspari, Brighenti & Temi 2012). Recently, Turner & Shabala (2015) and

* E-mail: v.mahatma2@herts.ac.uk

Hardcastle et al. (2019) inferred the bulk jet powers of the population of observed RLAGN from different radio surveys, assuming a distribution of radio galaxy environments based on cluster atmospheres and a particular lifetime function. While such inferences may be made for a population of sources, the jet power for any given source may be determined observationally by directly probing the jet energetics. Godfrey & Shabala (2013) estimate jet powers using hotspot luminosities, while Lobanov (1998) use the spatial shifts of the radio core in VLBI images, probing the parsec scale jets. To measure jet powers observationally for large samples, the simplest method in principle is to measure the total instantaneous energy output by the source (E_{total}), its lifetime (t_{age}) and taking their ratio ($Q_{jet} = E_{total}/t_{age}$). Methods of estimating E_{tot} and t_{age} are discussed below.

1.2 Energy estimates

Methods of directly estimating E_{total} have traditionally varied. For RLAGN in rich cluster environments, the lobes may excavate cavities in the hot X-ray emitting ICM, leading to large-scale decrements in the X-ray surface brightness, which enable *pdV* estimates of the work done by the lobes on their surroundings (Bîrzan et al. 2004; Rafferty et al. 2006). Such a calculation, however, may result in an underestimate of the total energy output by the jets – numerical simulations by Hardcastle & Krause (2013) and English, Hardcastle & Krause (2016) show that the energy contained in the lobes (through radiating and non-radiating particles) is estimated to be only half of the total energy ever injected by the jets, where the remaining energy is transferred into shock-heating the surrounding medium (see O'Sullivan et al. 2011 for a list of uncertainties regarding the use of cavity power estimates). Cavity power estimates have been used to derive a linear scaling relationship between jet power and radio luminosity, as found by Cavagnolo et al. (2010), but such a relation is bound to be unreliable for inferring the jet power for a given radio luminosity, as physical parameters such as the environmental density and the source age must also control the observed radio luminosity. Multiwavelength information describing the energetics of the radio lobes *and* its surrounding shocked material, applicable to all radio galaxies, can give more reliable estimates of E_{total}. Ineson et al. (2017) indeed use $E_{total} = 2E_i$, where E_i is the internal energy density of the lobes calculated directly using radio synchrotron and X-ray inverse-Compton measurements of a large sample of FR-II sources. Given a correct estimate of the source age, this would provide a reliable calculation of jet power.

1.3 Age estimates

Radio galaxy lifetime estimates can also be found in various ways: dynamical models which describe the speed of the radio jets, the lobes or their shocks have often been invoked in combination with the instantaneous source size to determine 'dynamical ages' (Kaiser & Alexander 1997; Kaiser, Schoenmakers & Röttgering 2000). As an alternative to dynamical ages, 'spectral ageing' can be used to determine the radiative ages of the relativistic electron population in radio galaxies, and has been used extensively as a tool to derive source ages from observations (e.g. Hargrave & Ryle 1974; Alexander 1987; Carilli et al. 1991; Shulevski et al. 2012) as well as from synthetic lobe radio spectra (Turner et al. 2017; Turner 2018). We discuss the usage and the validity of both methods below.

1.3.1 Dynamical ages

The determination of lobe advance speeds from observations has been attempted with X-ray observations: powerful jets drive a shock into their surrounding medium, heating their group or cluster media (Heinz, Reynolds & Begelman 1998; Kraft et al. 2007; Croston et al. 2009), and so X-ray measurements of physical conditions allow estimates of shock speed (e.g. Ineson et al. 2017). Alternatively, cavity power estimates often use the assumption that the lobes have expanded at the sound speed (Bîrzan et al. 2004, 2008; Cavagnolo et al. 2010). Both these methods have a clear drawback: the rate of expansion of the lobes is not constant, as radio lobes in general decelerate with time due to the interaction with their surrounding environment. Because the speed in the past is likely to be higher than its instantaneous value, these models overestimate the dynamical age.

Analytic models or numerical simulations (e.g. Hardcastle & Krause 2013; Turner & Shabala 2015; English et al. 2016; Hardcastle 2018) that aim to reproduce the observed properties of a particular source can circumvent problems with instantaneous measurements. However, numerical modelling requires jet power and environmental information as an initial condition. The use of a suite of different simulations to estimate jet power from observables would be possible in principle but computationally very expensive.

1.3.2 Spectral ages

The radiative ageing of electrons in the lobes of powerful radio galaxies occurs as follows. As the jet propagates into its environment, a strong shock (often termed reverse shock) develops at its termination point, which in turn accelerates particles to very high energies (Lorentz factors of $\sim 10^5$ or higher) through magnetic inhomogeneities in front of and behind the shock (Bell 1978). As a simple model, a single population of accelerated electrons at the same energy will leave the acceleration region as the jet advances, travelling downstream. These electrons, filling the radio lobe, will then suffer energy losses via the synchrotron, inverse-Compton, and adiabatic expansion processes. The loss time-scale for the synchrotron process goes as $\tau \sim 1/E$ and hence higher energy electrons radiate away their energy E more rapidly than lower energy electrons. This creates a characteristic observed radio spectrum which is a power law at low frequencies and curves downwards at higher frequencies. The spectral age is given by

$$t_{spec} = 50.3 \frac{B^{1/2}}{B^2 + B_{CMB}^2} \left((1+z)\,\nu_b\right)^{-1/2} \mathrm{Myr}, \quad (1)$$

(Leahy 1991), where B (nT) is the magnetic field strength in the lobes, B_{CMB} (nT) is the magnetic field strength in the cosmic microwave background, z is the sources' redshift, and ν_b (GHz) is the 'break' frequency where radiative losses begin to significantly affect the observed spectrum. Both the magnetic field strength and the break frequency are required parameters; the latter can be obtained directly from the observed radio spectrum.

The reliability of this method to accurately determine the age of radio galaxies is unclear. The spectral age is strongly dependent on the lobe magnetic field, the value of which has often been estimated using the argument that the energy density in the magnetic field is in equipartition with that in the radiating particles. While this assumption has been invoked for many years, inverse-Compton measurements. At least for Fanaroff–Riley type II (FR-II; Fanaroff & Riley 1974) sources, constrain the lobe magnetic

field strengths to be substantially lower than those implied by equipartition (Croston et al. 2005; Ineson et al. 2017). Furthermore, low-sensitivity, narrow-bandwidth observations from the previous generation of radio telescopes may not accurately trace the oldest radiating particles since last injection – a feature of the rapidly fading nature of synchrotron radiation that also prevents detections of switched-off radio galaxies even in sensitive low-frequency surveys (Brienza et al. 2016, 2017; Mahatma et al. 2018).

1.3.3 Outstanding questions

Even with current generation radio telescopes such as the Karl G. Jansky Very Large Array (VLA), with its high sensitivity and broad-band capabilities, and our improved understanding of the dynamical evolution and the energetics of the lobes, a discrepancy between the spectral and dynamical age of sources is still observed (Eilek 1996; Harwood et al. 2013; Harwood, Hardcastle & Croston 2015). Spectral ages are still being underestimated with respect to dynamical ages. This implies that the use of spectral ages to derive the jet power of RLAGN would overestimate the true kinetic power of the source, if the modelled dynamical ages are correct. Harwood et al. (2013, 2015; hereafter H13 and H15, respectively) investigated the spectral age/dynamical age problem of bright FR-II radio galaxies, developing the BRATS software package – a tool that derives spectral ages from radio maps from spatial regions determined on a pixel-by-pixel basis. This allows age estimates to be obtained as a function of distance along the lobes on a truly resolved basis, rather than integrating over large spatial regions as has been done in the past (e.g. Alexander & Leahy 1987). H15, using the BRATS package, still found that that their spectral ages can be underestimated by an order of magnitude with respect to their dynamical ages. Their use of equipartition estimates may have been the primary driver in the discrepancy, but they also used a simple power-law model for the environments; ideally environments would be constrained by observations. Moreover, subsequent studies have suggested that even the faintest radio emission from the lobes may trace a mixture of electron populations with different ages. Harwood et al. (2016) and Harwood (2017) predicted that electron mixing would be a contributing factor in determining spectral ages that may be biased towards younger populations. Turner et al. (2017) later confirmed these predictions with numerical simulations, showing that such electron mixing occurs progressively for the oldest material, strongly affecting the observed spectrum, and hence the spectral age. It is important to quantify observationally the effect of electron mixing.

A further uncertainty in spectral ageing comes from the choice of injection index, α_{inj}, the index of the initial power law injected by particle acceleration (H13, H15). Observations of hotspots have given values of around 0.5–0.6 for α_{inj} (Meisenheimer et al. 1989; Carilli et al. 1991) while shock theory predicts a value of 0.5 (Longair 2011). However, H13 and H15 found $\alpha_{inj} \sim 0.8$, while Harwood (2017) find $\alpha_{inj} \sim 0.7$ with broader coverage at low frequencies, suggesting that absorption processes or additional acceleration mechanisms may affect fitted measurements. While a lack of frequency coverage at low frequencies (~ 1.5 GHz) may cause the models to predict steeper injection indices, it may simply be the case that FR-II radio galaxies have a large spread of α_{inj}. Further studies are needed to understand the value and distribution of α_{inj}.

In general, it is crucial to understand whether physical or observational effects drive the dynamical/spectral age discrepancy. Deep observations of cluster-centre radio galaxies displaying large-scale shocks being driven by the expanding radio lobes into the surrounding environment, as well as high resolution and sensitive broad-bandwidth radio maps of the radio sources are necessary. This will allow us to capture the faintest and most aged electron populations in the radio lobes for a spectral ageing study, and with a reliable model for the dynamical advance of the radio lobes, we may investigate the cause of the spectral age/dynamical age discrepancy in detail.

There are, however, few observations of powerful sources driving shocks in their surrounding medium, due to the rarity of powerful sources at low redshift. So far, in addition to Cygnus A, there are only a handful of FR-II sources with X-ray observations showing a central shock being driven by the lobes, while a much larger population of the lower power FR-I systems interacting with the central parts of the cluster are known. Recently, VLA observations of the nearby young FR-I radio galaxy NGC 3801, which drives a shock seen in the X-ray (Heesen et al. 2014), have shown that the spectral and dynamical ages agree to within a factor of two. However, there is also significant evidence for *in situ* particle acceleration and/or mixing of the electron population in the lobes. It is unclear how well this generalizes to much more powerful and physically larger objects such as FR-IIs which are better understood in terms of their dynamics – classical doubles are routinely modelled, both analytically and numerically, to predict their physical properties as well as the impact on to their environments (e.g. Scheuer 1974; Kaiser & Alexander 1997; Hardcastle & Krause 2013; English et al. 2016). As the predictions of these models are tested by detailed observations, the subsequent refinement of these models may also be used to predict properties of radio galaxies and their impact at high redshift. Low-redshift observations are ideal for these studies due to the sensitivity and resolution requirements.

In this paper, we present high resolution, sensitive radio and X-ray observations of two FR-II cluster-centre radio galaxies in order to investigate the spectral age/dynamical age problem. By constraining the source physical parameters using these observations, we determine spectral ages using the techniques of H13 and dynamical ages using an analytic model to investigate the spectral age/dynamical age problem. In Section 2, we describe our observations and their data reduction. Section 3 describes the techniques we employed to extract physical parameters of our sources, the fitting of spectral ages to our observations and the analytic modelling leading to robust dynamical ages. In Section 4, we summarize our results and discuss their implications, followed by our main conclusions in Section 5. Some of the results presented in this paper have been reported previously as part of a research degree thesis (Mahatma 2017).

Throughout this paper we define the spectral index α in the sense $S \propto \nu^{-\alpha}$. We use a ΛCDM cosmology in which $H_0 = 71$ kms^{-1}Mpc^{-1}, $\Omega_m = 0.27$, and $\Omega_\Lambda = 0.73$.

2 OBSERVATIONS

We require good quality observations of source environments in order to model their dynamical evolution. To add to the difficulty in obtaining such extensive observations, the fact that not all radio galaxies with the best radio observations necessarily drive observable shocks in their external medium means that the number of potential sources available to be observed is severely limited, particularly at low redshift where FR-II sources are less common in dense environments. It is more efficient to initially cross-match bright sources found in radio surveys with X-ray surveys, followed by targeted deep X-ray observations of the shock, followed by high resolution and broad-band radio observations, rather than vice

versa. 3C 320 and 3C 444 were both selected initially from unbiased *Chandra* X-ray snapshot surveys of powerful radio galaxies by Massaro et al. (2013) and Mingo et al. (2014), respectively, showing clear shock signatures (i.e surface brightness jumps around the lobes). Both sources were thus selected for deeper follow-up X-ray observations using *Chandra* and *XMM–Newton* for 3C 320 and 3C 444, respectively. For the radio follow-up, both targets were observed with the VLA in multiple array configurations for good *uv* coverage and for broad-bandwidth data at 1.5 GHz (*L* band; 1 GHz bandwidth) and at 6 GHz (*C* band; 4 GHz bandwidth). Below, we describe the observations in detail for each source, followed by a description of the imaging processes.

2.1 3C 320

3C 320 is an intermediate redshift ($z = 0.342$) classical FR-II radio galaxy, hosted by a brightest cluster galaxy located in the centre of a rich cluster as inferred from its X-ray emission (Massaro et al. 2013). 3C 320 was selected as one of the brightest cluster galaxies (BCGs) in its respective survey and followed up with deep *Chandra* observations, summarized in Table 1. These observations, taken for the present project, have already been analysed by Vagshette, Naik & Patil (2019), who find large X-ray cavities in the ICM associated with the radio lobes, and weak shocks surrounding the lobes.

The corresponding radio observations were made using the VLA at *L* band in A-configuration (1.3 arcsec synthesized beam) and with e-MERLIN[1] for longer baseline data[2] (0.15 arcsec synthesized beam), leading to a comparable combined angular resolution (∼0.5 arcsec) to that provided with the *C*-band observations, made with the combined VLA A-configuration and B-configuration data (∼0.7 arcsec beam). These radio observations are summarized in Table 2.

2.2 3C 444

3C 444 is a nearby ($z = 0.153$) FR-II radio galaxy, hosted by an elliptical galaxy surrounded by a diffuse halo (as detected with Gemini GMOS-S; Ramos Almeida et al. 2011) at the centre of the cluster Abell 3847. Direct evidence for shock heating by the lobes of 3C 444 probed by X-ray observations of the hot ICM has been given by Croston et al. (2011) and Vagshette et al. (2017) – in the former study, 3C 444 was selected serendipitously as part of a programme observing the southern 2Jy sample of radio galaxies (Morganti, Killeen & Tadhunter 1993).

Unlike the case for 3C 320, the snapshot *Chandra* data for 3C 444 were deep enough to constrain the shock and Croston et al. (2011) obtained a dynamical age, modelling the instantaneous shock Mach number directly using the X-ray emission. While these data are sufficient to measure the central shock properties, as analysed in Section 3.1.1, for our analytic modelling (Section 3.3) we required more sensitive observations displaying the larger scale outer environment around the shock. Deeper observations were made with *XMM–Newton* of the larger scale structure of the ICM, and are used to model the predicted central ICM properties in Section 3. The *Chandra* and *XMM–Newton* observations are summarized in Table 1.

For the follow-up radio observations, the longest VLA baselines were sufficient to resolve the small-scale structures (i.e. the radio

core and hotspots) and we did not require the longer baselines of e-MERLIN, owing to the fact that 3C 444 is larger than 3C 320 in angular size. At *L* band, 3C 444 was observed in the A and B-configuration, and at *C* band, we used the B and C-configuration. The observations are summarized in Table 2.

2.3 Data reduction and imaging

2.3.1 Radio data

For the VLA data, the data reduction was performed using the *Common Astronomy Software Applications* (CASA) package version 4.7.1, in the standard manner, for both 3C 320 and 3C 444. The measurement sets for each VLA array at each observing frequency (*L* and *C* band) were reduced individually and manually using the standard CASA routines. The 3C 320 e-MERLIN *L*-band data set was reduced using the e-MERLIN CASA pipeline.[3] Prior to any data reduction tasks the flagging framework AOFlagger (Offringa, van de Gronde & Roerdink 2012) was used to flag channels with radio-frequency interference (RFI). Flagging bad antennas that were stated in the VLA observers log was carried out only if erratic phase and amplitude gain solutions were derived for the same antennas.

Prior to initial phase and bandpass calibration, the most recent model flux densities of 3C 286 and 3C 48 (for 3C 320 and 3C 444, respectively) were applied to the flux calibrator observations using the scale of Perley & Butler (2013). Antenna delay, bandpass, phase, and amplitude gain calibrations were performed, applying the previous calibration solutions on the fly for better calibration. The CASA rflag algorithm was also used on the data sets to remove residual RFI after applying the calibration tables.

The CASA task CLEAN (Högbom 1974) was used as the deconvolution algorithm for imaging. This task was used to combine the various VLA array data at *L* and *C* band in the *uv* plane, as well as the *L*-band VLA and e-MERLIN data for 3C 320, during the deconvolution process to produce high-fidelity broad bandwidth images, as shown in Fig. 1. Most of the default CASA CLEAN parameters were kept, bearing in mind that we require emphasis on image fidelity, showing both compact structures and the diffuse large-scale (ageing) structure. Hence, we performed multiscale cleaning and multifrequency synthesis, owing to our broad-bandwidth data, and cleaned down to 0.01 mJy. A list of parameters used, and their values, are given in Table 3. For 3C 444, the imaging parameters were consistent across the *L*-band and *C*-band data, using a Briggs robust weighting parameter of 0.0 in order to keep the optimum weighting for the visibilities. For 3C 320 at *L* band, we did not require manual re-weighting of the individual e-MERLIN and VLA data sets relative to one another in order to view both compact and large-scale structures, as would generally be required for telescopes with different sensitivities. However, since the core and hotspot emission were much more prominent in the e-MERLIN data, during the imaging we increased the weights of the longest baselines in the combined data, using a robust value of −0.8. We were consequently required to image the VLA *C*-band data with a robust value of −2.0 to match the 0.5 arcsec synthesized beam of the e-MERLIN data at *L* band.

Self-calibration was performed for the individual array data for both 3C 320 and 3C 444 before combination. Phase gain solutions were derived with 30 s solution intervals assuming a reference antenna near the geometric centre of the array configuration. Only

---

[1] http://www.e-merlin.ac.uk
[2] Without the Lovell Telescope.

[3] https://github.com/e-merlin/eMERLIN_CASA_pipeline

Table 1. X-ray observations of 3C 320 and 3C 444. The observation ID refers to IDs for the multiple data sets taken, if any.

Source	Telescope	Observation ID	Chip	Energy band (keV)	Observation date	Duration (ks)
3C 320	*Chandra*	16130,16613	ACIS-S	0.5–7.0	2014-05-11	110
3C 444	*XMM–Newton*	0691840101	MOS1, MOS2, PN	0.3–7.0	2012-11-16	134
	Chandra	15091	ACIS-S	0.5–7.0	2014-04-12	164

Table 2. Radio observation details of 3C 320 and 3C 444. The 'Project ID' refers to the project name for the VLA and e-MERLIN data. 'Array' gives the VLA array configuration used for each observation at *L* band (1.5 GHz) and *C* band (6 GHz), or the antennas used in the case of the e-MERLIN observations. The 'Duration' refers to the approximate total observation time including all the calibrator sources.

Source	Project ID	Array	Frequency (GHz)	Observation date	Duration (h)	Flux calibrator
3C 320	15A–420 (VLA)	A	1.5, 6	01/08/15	4	3C 286
		B	6	15/02/15	1.5	
	CY4223 (e-MERLIN)	Mk2,Pi,Da, Kn,De,Cm	1.5	22/03/18	16	3C 286
3C 444	15A–420 (VLA)	A	1.5	18/06/15	3.5	3C 48
		B	1.5, 6	07/02/15	4	
		C	C	31/01/16	1.5	

one iteration of amplitude self-calibration was performed after phase self-calibration, with further iterations degrading the image quality.

2.3.2 X-ray data

Two separate *Chandra* observations of 60 and 50 ks for 3C 320 were made, and reprocessed using the Chandra Interactive Analysis of Observations (CIAO; Fruscione et al. 2007) software package from the level 1 events files with CIAO 4.7 and CALDB 4.6.7. The *chandra_repro* pipeline was subsequently used to reprocess the data to produce new level 2 events files using standard CIAO analysis methods. For analysis, the merged events files were initially filtered to allow counts between 0.5–7 keV. The observations were then combined before spectroscopic analysis. The *Chandra* observations for 3C 444 presented by Croston et al. (2011), which we use in Section 3.1.1, were processed in a similar way with CIAO 4.6.1 and CALDB 4.6.4.

The *XMM–Newton* events files for 3C 444 were reprocessed with the latest calibration data using *XMM–Newton* SAS v11.0.0. The pn camera data were filtered to include only single and double events (PATTERN 4), and data from the MOS cameras were filtered using the standard pattern mask (PATTERN 12). The data sets were also filtered to remove bad pixels, bad columns, etc. We checked each events file for flares using the light curves at higher energy levels than those emitted by the sources and used good-time-interval (GTI) filtering to select data where the light curve was within 20 per cent of the quiescent level. We then used evigweight to correct the events files for vignetting. The particle background in the *XMM–Newton* sources was removed using the method described by Croston et al. (2008). This uses closed filter files that were processed, filtered, and weighted in the same manner as the source data sets. The closed filter data were rotated to match the source observations, and scaling factors were calculated by comparing the count rates of the pn and MOS cameras. The closed filter data were then scaled by these factors before carrying out background subtraction when generating profiles and spectra.

We generated images for the *XMM–Newton* sources using the method described by Croston et al. (2008). An image was extracted for each of the three EPIC cameras using evselect. The MOS images were then scaled to make their sensitivity equivalent to the pn camera image so that there would be no chip-gap artefacts when the three images were combined. We generated exposure maps for each camera using eexpmap, which were used to correct for the chip gaps, but not for vignetting as this leads to incorrect scaling of the particle background that dominates at large radii. The resulting image is therefore not vignetting corrected; it is purely pictorial and not used in any subsequent analysis.

The *Chandra* and *XMM–Newton* images of the large-scale environments surrounding 3C 230 and 3C 444, respectively, are shown in Fig. 2. These figures have been produced using the *Chandra* Imaging and Plotting System (CHIPS).

3 ANALYSIS

In this section, we present the methods used to determine the spectral and dynamical ages of 3C 320 and 3C 444. We first describe our methods of obtaining constraints on physical parameters that are required for the spectral ageing and dynamical age calculations; these are the ICM shock properties, the immediate and larger scale environments and the lobe magnetic field strength of the sources. We then proceed to describe our methods to obtain spectral ages, followed by modelling the dynamics of both sources to obtain their dynamical ages.
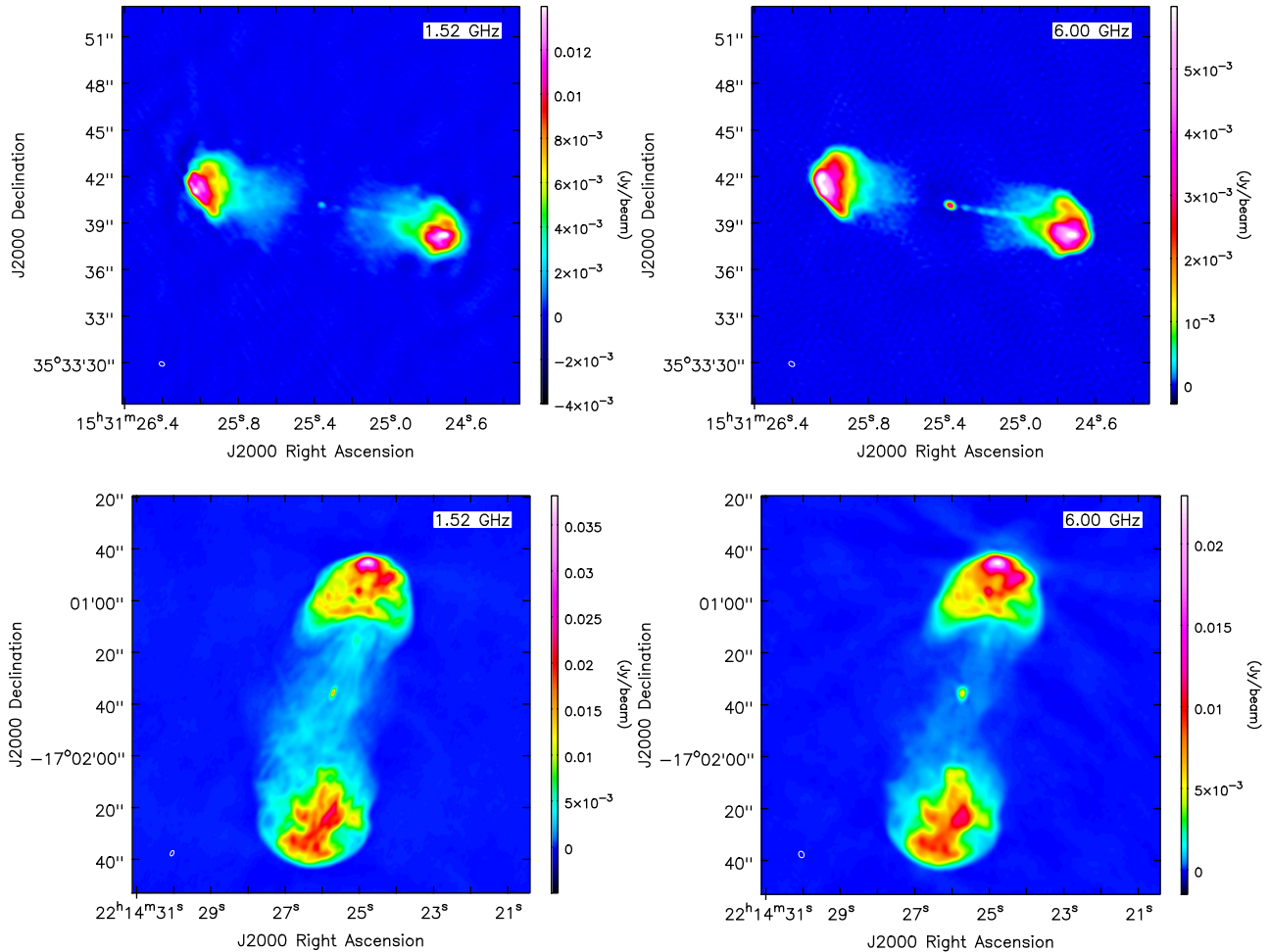
Figure 1. VLA images of 3C 320 (upper row) and 3C 444 (lower row), at *L* band/1.5 GHz (left column) and *C* band/6 GHz (right column). Images shown are the final self-calibrated and array-combined broad-band data sets (see text). For 3C 320 the beam sizes are 0.35 × 0.27 arcsec (left) and 0.57 × 0.40 arcsec (right). For 3C 444 the beam sizes are 2.2 × 1.3 arcsec (left) and 2.6 × 2.1 arcsec (right). Beam shapes are shown on the lower left of each image panel. The pixel sizes are 0.1 arcsec for 3C 320 (both), and 0.3 arcsec (left) and 0.4 arcsec (right) for 3C 444. Residual rms levels are ∼50 μJy beam^{-1} (left) and ∼47 μJy beam^{-1} (right) for 3C 320, and ∼25 μJy beam^{-1} (left) and ∼15 μJy beam^{-1} (right) for 3C 444. The colour bar in each image has scaled appropriately to display both compact and diffuse structures.

Table 3. Clean parameters used in CASA to image the 3C 320 and 3C 444 data at *L* and *C* band. Where different parameter values were used, we simply state the range. 'Beam' refers to the synthesized beam. Most default parameters are not listed.

| Clean keyword	Value
threshold	0.01 mJy
psfmode	'clark'
mode	'mfs'
imagermode	'csclean'
ftmachine	'mosaic'
multiscale	0, 2, 5, 10 × beam
robust	−0.8–0.0

3.1 Source physical properties

3.1.1 Shock measurements

To determine the physical properties of the shocked X-ray emitting ICM surrounding 3C 320 and 3C 444, we extracted the spectrum from the calibrated *Chandra* data (we used the archival *Chandra* observations analysed by Croston et al. 2011 rather than the *XMM–Newton* observations for 3C 444 as presented in Fig. 2, to better constrain the shock with higher angular resolution). Count rate files were extracted from the merged events files on two regions of interest; the centrally shocked medium, defined as the central region bounded by a visually clear surface brightness jump, and a background region defined as an annulus directly around the shock (see Fig. 3). We used the CIAO software package to obtain spectra for these regions and SHERPA for spectral fitting.

Bad data were removed using the ignore_bad() command, removing bins based on bad data flags. The data were then filtered in the energy range 0.5–5.0 keV and 0.5–7.0 keV for 3C 320 and 3C 444, respectively – allowing a larger energy range for the 3C 320 observations resulted in poor fits when analysing the individual lobe regions as described in Section 3.1.3, and hence we keep the energy range analysed for the shock and lobe regions consistent. Background emission was subtracted based on the count rates in the immediate vicinity of the shock (dashed lines in Fig. 3).
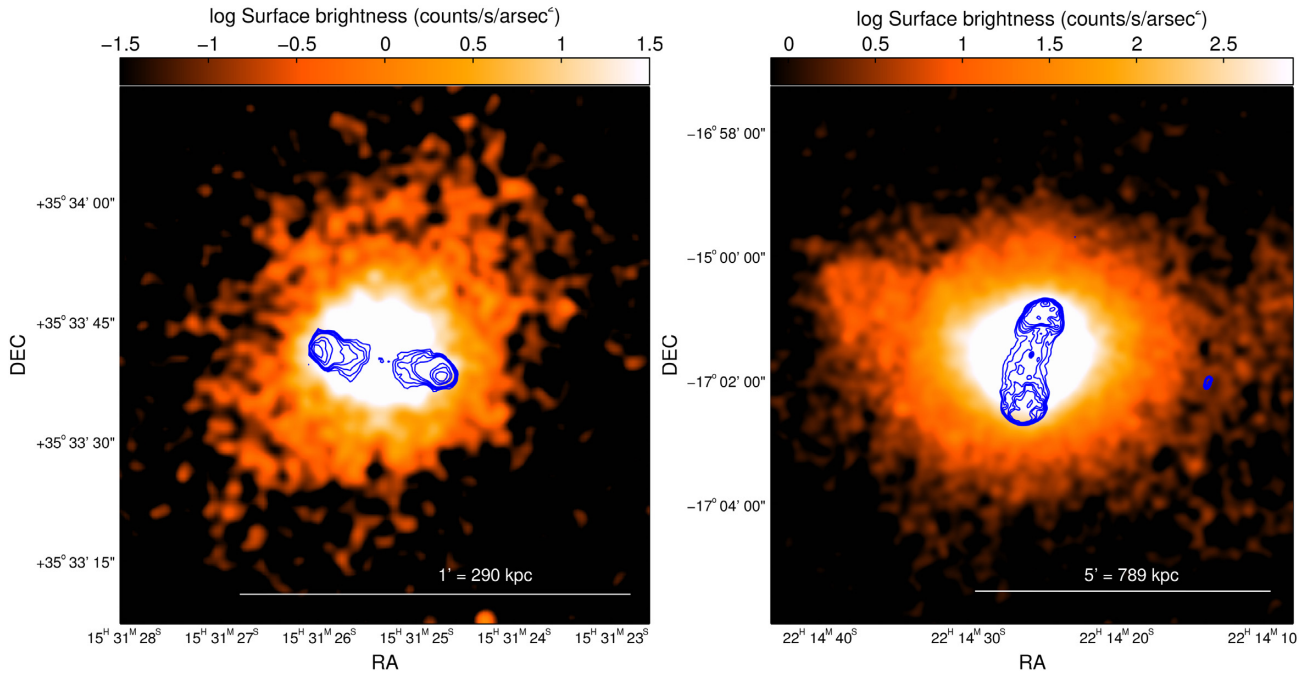
Figure 2. X-ray *Chandra* (left) and *XMM–Newton* (right) observations tracing the hot gas of the ICM surrounding 3C 320 and 3C 444, respectively. Images have been scaled using a logarithmic transfer function, allowing the sharp X-ray surface brightness increase around the radio source (the shock) to be seen clearly. Overlaid are 1.5 GHz contours of the radio source given by our VLA observations. The contour levels in this figure have been chosen to emphasize the radio structures clearly.

For both regions, a thermal *APEC* model was fitted to the spectra, describing thermal emission from collisionally ionized diffuse gas, and such a spectrum is expected from the X-ray emitting gas of the intracluster medium. A photoelectric absorption model was also added as a multiplicative component to the *APEC* model to account for the absorption of X-ray photons by foreground atomic matter such as hydrogen atoms in cold gas. An added non-thermal power-law emission model was also tested for the shock region, as would be expected due to non-thermal processes such as inverse-Compton scattering from the radio source, but resulted in worse fits and also a non-detection of non-thermal emission, and hence we considered only the absorbed thermal model to describe the shock. The Galactic absorbing column density was fixed at 1.64×10^{20} atoms cm^{-2} and 2.51×10^{20} atoms cm^{-2} (based on previous observations) as well as the redshift at 0.342 and 0.153 and the elemental abundance at $0.3\times$ solar, for 3C 320 and 3C 444, respectively. The only free parameters for the thermal model were the temperature and normalization. The best-fitting values for the physical parameters of the fitted models for the shocked medium are tabulated in Table 4. The background-subtracted spectra for the shock regions and their best-fitting thermal models (solid red line) are shown in Fig. 4. The electron density n_e is directly calculated using the fitted normalization to the thermal APEC model;

$$\mathrm{norm} = \frac{10^{-14}}{4\pi \left(D_A \left(1+z\right)\right)^2} \int n_e n_H \mathrm{d}V, \qquad (2)$$

where D_A is the angular diameter distance, z is the redshift, and n_H is the number density of hydrogen atoms. We compute the integral in equation (2) analytically since we have determined volume-averaged parameters and we can make the assumption that $n_e/n_H \approx 1.2$. Hence, we only need to compute $\int \mathrm{d}V = V$, for the shocked regions shown in Fig. 3.

Region volumes were initially determined using projected angular sizes – the projected shocked region for 3C 320 was fitted as a circle, leading to a calculation of the volume of a sphere with the radius defined as shown in Fig. 3. For the more complex 3C 444, the projected emission is in the form of an ellipsoid, and hence the true physical volume may be different from the projected volume depending on the orientation angle to the line of sight. We assume the physical depth to be equal to the projected minor axis (i.e. a prolate spheroid), as typically modelled for the shock in dynamical models (e.g. Hardcastle 2018). To determine the geometrical uncertainties due to orientation, we determine plausible upper and lower limits of the major axis. The projected major axis can never be larger than the physical major axis, and hence the lower limit volume of the shocked shell is obtained when we use the projected major axis. The shocked shell may then be any orientation angle to the line of sight, but since we observe double radio lobes which imply that the source is at a large angle to the line of sight, we place a lower limit on the orientation angle of 45° to the line of sight. The upper limit volume uses the upper limit major axis, which is the projected length divided by cos(45°). For both sources, the projected lobe volumes were subtracted from the shock volume (orientation effects of the lobe sizes on the lobe-subtracted shock volume are considered in Section 3.3), as we only consider emission from the shocked ambient medium. We also subtracted the volume of a 'cold bar' of emission seen over the core of 3C 320, and the central AGN point source of 3C 444 (masked out regions with a red diagonal line in Fig. 3). Electron densities, shock volumes, and fitted model temperatures for 3C 320 and 3C 444 are given in Table 4.

3.1.2 Central environment

Here we describe the extraction of the environmental properties of 3C 320 and 3C 444 from our *Chandra* and *XMM–Newton*
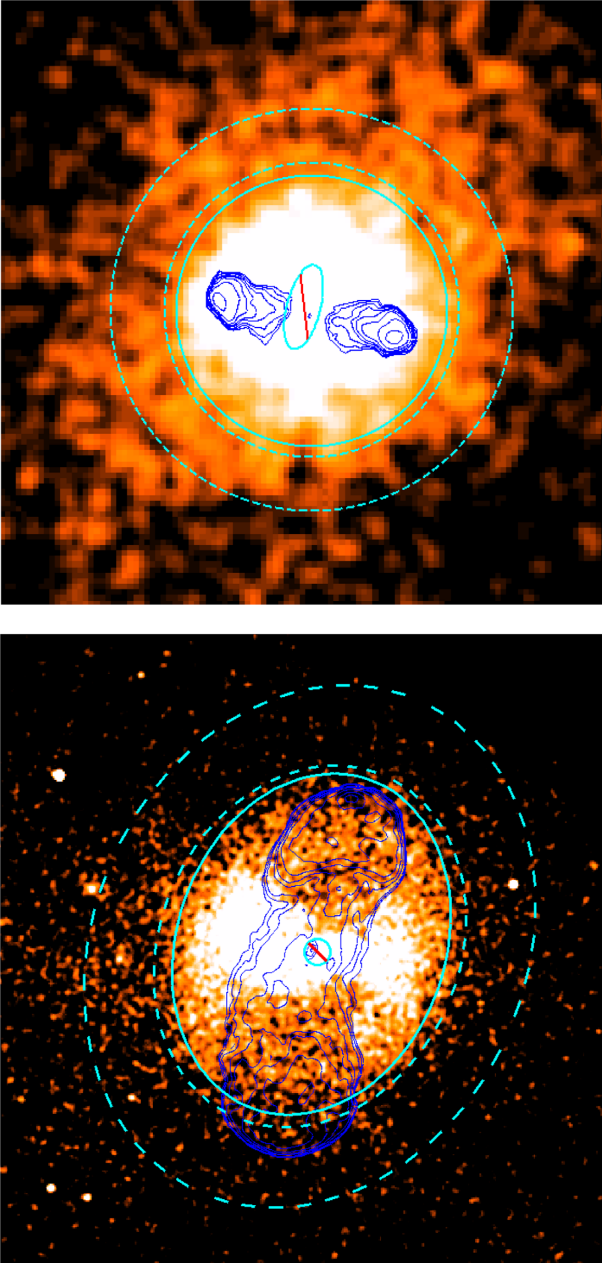
Figure 3. *Chandra* X-ray maps for 3C 320 (top) and 3C 444 (bottom), with radio source contours in blue from our VLA 1.4 GHz radio observations overlaid, showing regions (cyan) used to measure the ICM shock. Solid cyan lines represent the region used to extract spectra for the shock, and dashed cyan annuli represent the region used for background subtraction. The central ellipse and circle with a diagonal red line show the central AGN-related components masked out in our analysis for 3C 320 and 3C 444, respectively.

X-ray observations of the ICM, respectively. In particular, for the environment input parameters of the analytic model which will later be used to determine dynamical ages (Section 3.3), we require the ICM thermodynamic properties at the time the radio source switched on. Assuming the hot gas from the ICM can be well described by an isothermal beta model (Cavaliere & Fusco-Femiano

1978), where

$$p = p_0 \left[1 + \left(\frac{r}{r_{\rm c}} \right)^2 \right]^{-\frac{3\beta}{2}}, \qquad (3)$$

for the analytic model, we require the constant environmental temperature (kT), central pressure (p_0), core radius ($r_{\rm c}$) of the ICM, and the beta index (β), at $t = 0$. Directly fitting emissivity models to the integrated instantaneous X-ray emission (Fig. 2) would not necessarily translate to the true thermodynamic state of the ICM at the time the radio source switched on: shock heating by the radio source occurs throughout the source lifetime, as expected since this is suggested to be the main mode of feedback for cluster-centre radio galaxies, essentially removing information on the past history of the central parts of the ICM. We therefore fitted an isothermal beta model only to the outer un-shocked regions of the ICM, and extrapolated the best-fitting model down to the central region, which we assume will give estimates of the central density and pressure of the ICM in its undisturbed state.

As X-ray surface brightness scales with the square of the particle density, we directly obtained surface brightness profiles to the X-ray emission of the un-shocked media of 3C 320 and 3C 444 using tools from the FUNTOOLS library (Mandel, Murray & Roll 2001), defining concentric annuli outside the central shock. The first annulus was chosen to be directly outside the clear central shock region, with the annuli increasing in width out to the extent of the ICM, shown in Fig. 5. We masked chip gaps in the data (shown as red polygons), more so for the 3C 444 *XMM–Newton* data due to its larger field of view. After obtaining the radial surface brightness profiles to the un-shocked environment, we used the Markov Chain Monte Carlo (MCMC) algorithm (as described by Croston et al. 2008 and Ineson et al. 2013) to determine the best-fitting beta model to the profiles with four unknown parameters; the psf normalization, surface brightness normalization, β and $r_{\rm c}$, restricting the range of the parameter spaces to be within physically plausible values. An isothermal beta model was well fitted to the data points for the unshocked medium for both 3C 320 and 3C 444, with $\chi^2_{\rm red} \sim 1$ for the best-fitting models, shown in Fig. 6. It can be seen by the residuals (lower panel of the profiles) that the models are not well fitted to the first data point of the profile, i.e. the first annulus. This is due to the fact that most of the area of the first annulus is masked by the central shock, and hence any measurement should not be used as a 'true' measurement – we arbitrarily increased the count rate error for the first data point of the 3C 444 *XMM–Newton* data to reflect this, essentially removing it as a measurement from the fit.

To obtain a value for the isothermal cluster temperature, we fitted a thermal APEC model to the *Chandra* and *XMM–Newton* X-ray emission spectra (between 0.5–5 keV and 0.5–7 keV for 3C 320 and 3C 444, respectively), masking out only the central shock, using the CIAO software package, giving best-fitting temperatures of $2.77^{+2.26}_{-0.85}$ and $2.33^{+0.10}_{-0.10}$ keV for 3C 320 and 3C 444, respectively. Given the central density output by the beta model and the fitted ICM temperature, we then use the ideal gas equation to determine the central pressure p_0. The physical environmental properties we derive are then used as input to the analytic model, used to model the evolution of 3C 320 and 3C 444, described in Section 3.3. Though we have outlined some of the assumptions used in this method in predicting the past state of the ICM, which may deviate from the true ICM properties in reality, our methods are physically motivated and represent the best possible approach with the available data.

Table 4. Shock physical properties for 3C 320 and 3C 444 based on our *Chandra* observations. All uncertainties are based on 3σ measurement errors, with the exception of the volume uncertainties for 3C 444, calculated using geometrical arguments. Note that we do not have volume uncertainties due to projection effects for 3C 320 due to its circular shock region. See Section 3.1.1 for more details.

Region	χ^2_{reduced}	kT (keV)	Norm ($\times 10^{-4}$)	n_e ($\times 10^2 (\text{cm}^{-3})$)	Volume $\times$ 10^{70} cm^3
3C 320	0.841	$3.488^{+0.700}_{-0.542}$	$2.138^{+0.176}_{-0.164}$	1.640 ± 0.065	2.033
3C 444	0.960	$2.845^{+0.150}_{-0.140}$	$15.534^{+0.278}_{-0.278}$	$0.680^{+0.537}_{-0.154}$	$18.831^{+7.800}_{-0.000}$
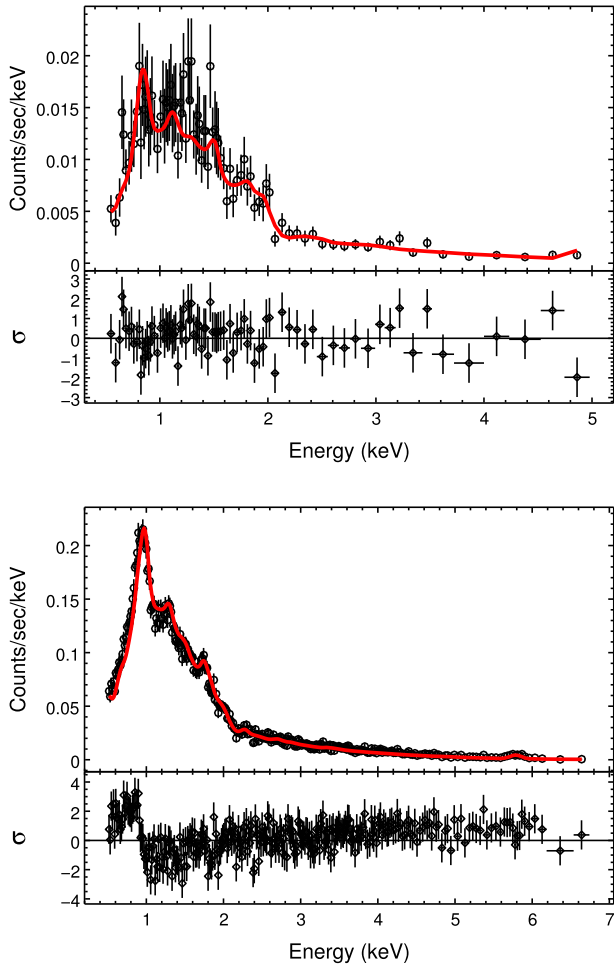
Figure 4. *Chandra* X-ray spectra for the background-subtracted shock region for 3C 320 (0.5–5 keV;top) and 3C 444 (0.5–7 keV;bottom) as defined in Fig. 3. The red solid line indicates the best fit absorbed thermal APEC model to the data. The lower panel in each figure indicates the reduced χ^2 statistic at each data point.

3.1.3 Lobe magnetic field strength

As stated in equation (1), the calculation of a spectral age requires a magnetic field strength, as one of the important parameters that govern the strength of radiative losses for a given electron energy, and the magnetic field strength is therefore an input parameter for the spectral age model fitting. As discussed in Section 1.3.2, equipartition estimates are likely to overestimate the true magnetic field, and inverse-Compton constraints are desirable. We used our *Chandra* X-ray observations of the ICM surrounding 3C 320 to search for inverse-Compton emission from the lobes, and a similar method was used to determine the field strength for 3C 444 by
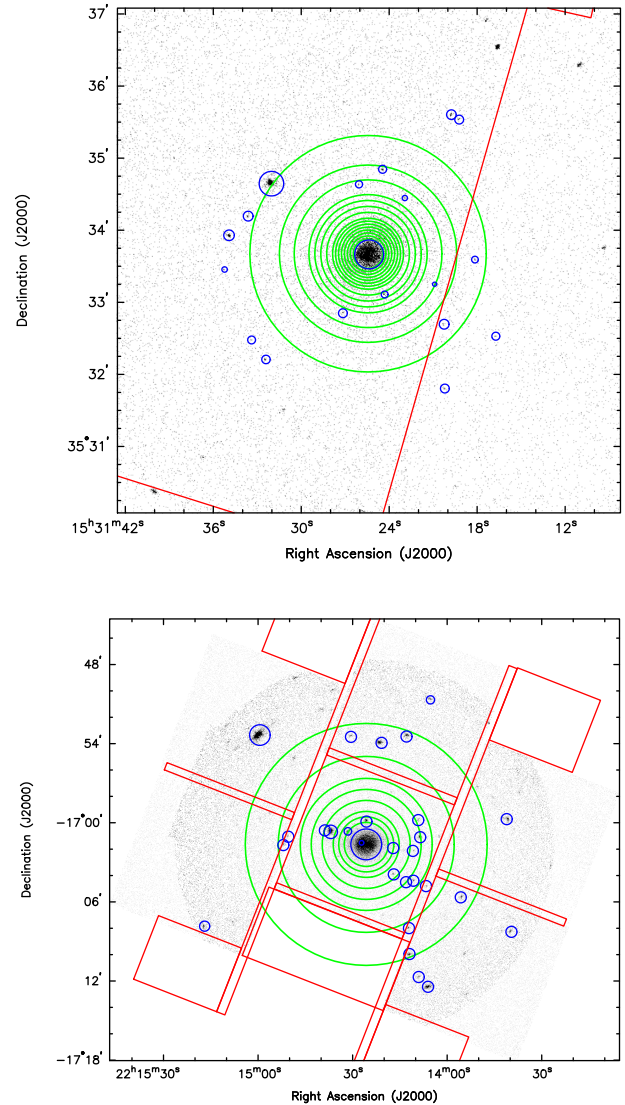
Figure 5. Concentric annuli (green) used to extract radial profiles from the X-ray observations of the ICM surrounding 3C 320 (top) and 3C 444 (bottom). Masked regions for point sources and the central shock are shown in blue. Regions omitted due to chip gaps are shown as red polygons. For clarity, the region to the right of the vertical red line for 3C 320 (top) marks a chip gap.

Croston et al. (2011) – we simply state their results here. We expect the dominant source of emission in our observations at the location of the radio source to be thermal bremsstrahlung rather than non-thermal inverse-Compton emission directly from the lobes – the shock region is physically larger than the lobes and includes the
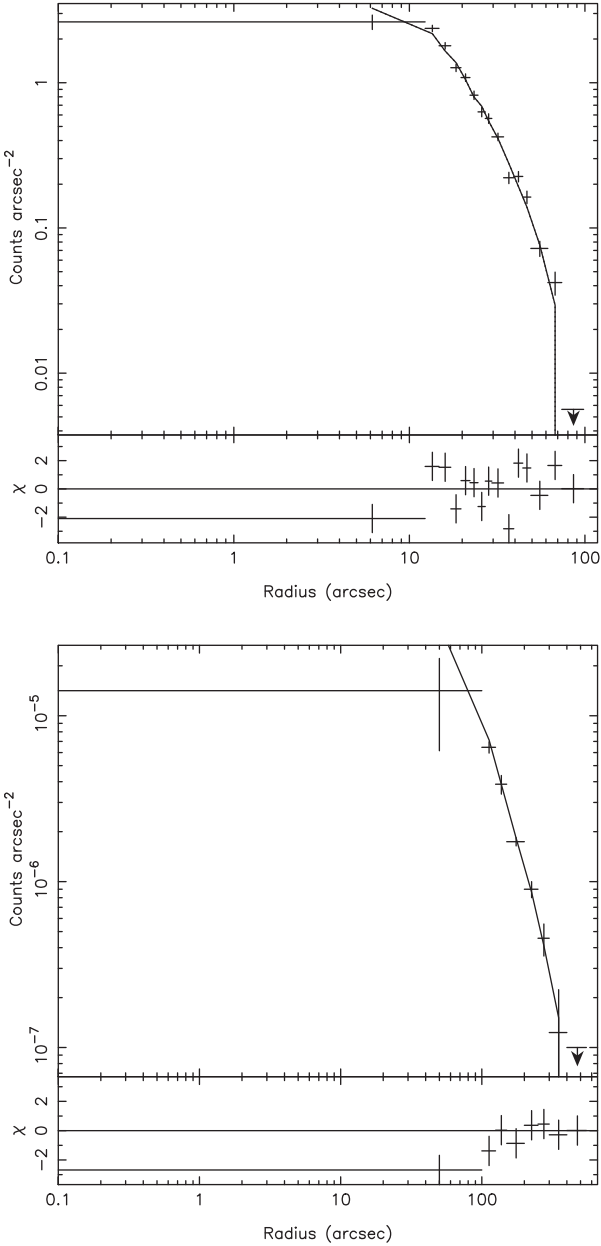
Figure 6. Radial surface brightness profiles for the outer (un-shocked) ICM for 3C 320 (top) and 3C 444 (bottom). The solid lines indicate the best-fitting beta model, with the residual χ^2 values in the lower panel of each figure.

integrated line of sight emission through the cluster, consisting of thermally emitting material. Moreover, it is difficult to entirely remove thermal foreground cluster emission in front of the lobes using only background subtraction, and hence any spectral-based fitting of non-thermal models on large regions is expected to be contaminated with thermal emission (e.g. Hardcastle & Croston 2010). We used the *Sherpa* application on the CIAO software to fit thermal and power-law models to elliptical regions at the location of both radio lobes in the *Chandra* observations. As the power-law model contains additional free parameters (the photon power-law index Γ and the corresponding normalization), we fixed the lobe temperature to that of the fitted temperature of the shocked medium found in Section 3.1.1, reducing the number of free parameters while keeping our analysis consistent. Initial fits resulted in Γ

Table 5. Emission model fits to the ICM, spatially coincident with the lobes of 3C 320. Regions modelled with an absorbed power-law model plus thermal APEC model with fixed values of $\gamma = 1.75$, thermal abundance at $0.3 \times$ solar and the temperature at the fitted shocked temperature of 3.488 keV. γ is defined in the sense $A(E)E^{-\gamma}$. Note that the power-law normalization was set such that it returns the 1 keV flux density in units of μJy. Flux densities are given as 3σ upper limits.

Lobe	χ^2_{red}	PL Norm	Thermal Norm	Flux density (nJy)
East	0.973	$0.000^{+0.0022681}$	$0.420^{+0.050}_{-0.176}$	<2.268
West	0.653	$0.000771^{+0.00522}$	$0.531^{+0.113}_{-0.531}$	<6.000

Table 6. Derived magnetic field strengths for the lobes of 3C 320 (this work) and 3C 444 (Croston et al. 2011). The upper limits are calculated using the equipartition assumption and the lower limits are based on the upper-limit inverse-Compton measurements.

Source	Upper limit (nT)	Lower limit (nT)
3C 320; east lobe	4.41	0.60
3C 320; west lobe	4.47	0.35
3C 444	1.05	0.50

being relatively unconstrained by large errors. Subsequent fitting with a fixed power-law index resulted in consistent values for the power law and thermal normalizations and the fitted χ^2_{reduced} for $1.5 \leq \Gamma \leq 2.0$. We therefore fixed the power-law index at $\Gamma = 1.75$ to improve the fitting (consistent with typically measured spectral slopes of radio lobes of $\alpha \sim 0.7$, as $\Gamma = \alpha + 1$). The results for the emission model fits for both lobe regions in the shock are given in Table 5.

As detailed in Table 5, we were not able to detect a non-thermal power-law component in the lobe regions of the cluster emission. A 3σ upper limit flux density of inverse-Compton emission was obtained, giving flux densities of 2.268 and 6 nJy for the eastern and western lobes, respectively. These are still within the range of detected inverse-Compton fluxes obtained for the lobes of FR-II galaxies (Erlund et al. 2006; Goodger et al. 2008).

We used the SYNCH code (Hardcastle, Birkinshaw & Worrall 1998) to determine the equipartition lobe magnetic field based on the observed radio flux densities measured with our VLA observations, giving a field strength of $B_{\text{eq}} \approx 4.4$ nT for both lobes of 3C 320 (assuming $\alpha_{\text{inj}} = 0.60$ for the low-frequency radio data as the expected value between the theoretical and steeper values from recent studies – the calculated field strength is not largely dependent on this value). Since the code also predicts the inverse-Compton spectral energy distribution based on a fixed magnetic field, we fixed the magnetic field strength value and ran the fitting process for a range of field strengths lower than the equipartition value until the measured upper limit flux density at 1 keV was consistent with the model-predicted inverse-Compton spectral energy distribution at the same energy. The magnetic field giving this consistency was then treated as a lower limit to the lobe magnetic field based on inverse-Compton constraints. Thus, we obtained both a lower and upper limit (from equipartition) lobe magnetic field strength for 3C 320, as derived similarly for 3C 444 (Croston et al. 2011). The derived field strength limits are given in Table 6. Taking approximately averaged values, we take the field strength for both lobes to be within the range 0.50–4.44 nT. For 3C 444, Croston et al. (2011) obtain a magnetic field strength range of 0.5–1.0 nT. We use these constraints to the

lobe magnetic field to calibrate evolutionary models for 3C 320 and 3C 444 in Section 3.3.

3.2 Spectral age fitting

We fit spectral ageing models to the radio lobe spectra using the BRATS software package. The best-fitting ages for a given input magnetic field gives the break frequency, which we later use to re-determine spectral ages after constraining the magnetic field strengths from our limits using our analytic modelling. Essentially, for a given age and magnetic field, the model fluxes are computed numerically for each region in the radio map and quantitatively compared with the observed flux for the same regions at the frequency of the map, producing a set of χ^2 values. The best-fitting ages for each of the predefined and resolved regions in the map are then output (see H13 for further details).

The currently favoured models are the Jaffe–Perola (Jaffe & Perola 1973) and Tribble (Tribble 1993; Hardcastle 2013) models of spectral ageing, and we limit our analysis to these models (see H13, H15 and Harwood 2017 for results on comparisons between models). To determine the source flux density $S_{\nu, i}$ at each intermediate frequency i, we produced sub-band images from the broad-bandwidth observations of 3C 320 and 3C 444 seen in Fig. 1. We imaged each spectral window (our *L*-band data has 16 and our *C*-band data has 32), producing sub-band maps with 64 MHz bandwidth at *L* band and 128 MHz at *C* band. Note that for 3C 320 at *L* band, we only considered the central half of the VLA bandwidth (8 spectral windows with 64 MHz bandwidth) to match the bandwidth covered by e-MERLIN (512 MHz). A lack of sensitivity to small-scale structures drove our need to then combine spectral windows to produce only three maps at *L* band for 3C 320. Moreover, we only used the first 20/32 spectral windows at *C* band, due to the fact that the most diffuse structures that are detected at *L* band are not detected at these higher frequencies. We did not require a reduction of useable bandwidth for our 3C 444 data.

We convolved each of the sub-band maps across both *L* and *C* band with a Gaussian beam of the same shape and size, and hence, across the entire frequency range of our observations, we are limited to the resolution of the lowest frequency data. We used a circular beam of FWHM 0.8 arcsec for 3C 320 and 2 arcsec for 3C 444. Since the imaging and the phase self-calibration processes described in Section 2 can introduce small spatial shifts in the maps, we performed a pixel alignment procedure by fitting a Gaussian to the radio core in all of the sub-band maps using CASA. Using the mean pixel co-ordinates of the core, we aligned all the maps where the core was offset from this reference position. These sub-band maps were directly used as input to BRATS, which determined the lobe flux density from each frequency/map to produce a spectrum. The unknown physical parameters that are required by BRATS for the spectral age calculation are the lobe magnetic field strength and the low-frequency particle injection index. In Section 3.1.3, we obtained inverse-Compton and equipartition-based lower and upper limits, respectively, to the true lobe field, resulting in $0.5\,\mathrm{nT} \leq B_{3C320} \leq 4.4\,\mathrm{nT}$ and $0.5\,\mathrm{nT} \leq B_{3C444} \leq 1.05\,\mathrm{nT}$, the latter obtained by Croston et al. (2011). A factor of two difference in magnetic field will also result in a factor of two difference in the spectral age at a fixed break frequency (as $B \sim B_{CMB}$ – see equation 1), and hence we ran the spectral age fitting assuming three values for the magnetic field strength within the allowed limits. To determine the injection indices, we use the BRATS command `findinject`, which fits for the low-frequency power law of the spectra using spectral ageing models. The injection index fitting was

Table 7. Best-fitting maximum spectral ages for 3C 320 and 3C 444 for two ageing models. Values are given at three magnetic field strength values ranging from the lower to upper measured limits. Note that the errors quoted are only statistical errors on model fits, and are therefore represent lower limits to the true uncertainty in ages.

Model	Spectral age (Myr)		
	0.5 nT	1.0 nT	4.4 nT
3C 320 (JP)	$35.48^{+0.74}_{-0.82}$	$21.98^{+0.32}_{-0.63}$	$3.05^{+0.08}_{-0.07}$
3C 320 (Tribble)	$42.90^{+0.44}_{-1.99}$	$25.10^{+0.31}_{-0.23}$	$3.78^{+0.03}_{-0.10}$
	0.5 nT	0.7 nT	1.0 nT
3C 444 (JP)	$38.00^{+0.28}_{-0.20}$	$27.48^{+0.06}_{-0.50}$	$18.48^{+0.06}_{-0.13}$
3C 444 (Tribble)	$42.90^{+0.09}_{-1.03}$	$30.10^{+0.10}_{-0.23}$	$20.86^{+0.05}_{-0.09}$

performed for 3C 320 and 3C 444 using magnetic field strengths at 4.44×10^{-9} T, 1.00×10^{-9}, and 0.50×10^{-9} T, and 0.5 nT, 0.74 nT, and 1.05 nT, respectively. The best-fitting injection indices gave values around $0.6 \leq q_{inj} \leq 0.65$ for any choice of magnetic field strength, for both sources, for both the JP and Tribble ageing models. The subsequently fitted spectral ages for all three magnetic fields and for all three ageing models are given in Table 7, and in Fig. 7, we display spectral ageing maps for both sources using the Tribble model and the intermediate field strength from the aforementioned field strength limits. The best-fitting break frequencies based on the Tribble model for the oldest plasma detected are 1.7 and 3.4 GHz for 3C 320 and 3C 444, respectively.

The process of spectral ageing can be clearly seen in these maps, with a smooth variation from particles at the injection region with young or zero age, to older populations towards the base of the lobes. More than one region in each source other than in the hotspots is clearly seen to have young populations of radiating particles, which may be associated with jet knots created by the jet driving into locally dense gas. It is important to note that we are not sensitive to faint regions at high frequencies – in particular for 3C 320, it can be seen that the oldest regions that would exist in the vicinity of the core (seen at *L* band) are missing from the maps. We discuss the implications of this in Section 4. We also note that the flux density errors on each sub-band map used to determine the spectrum are likely to be underestimated – our data reduction and self-calibration on the broad-band data sets may correlate the flux density measurements between sub-band maps. A robust treatment of these errors would increase the errors on each flux density measurement by a factor of ~2 for the *C*-band points relative to the *L*-band points, increasing the leverage of the *L*-band data in fitting the spectra. While this would affect the fitted break frequency, we do not have accurate constraints on all possible systematic uncertainties, and so we use the standard VLA flux calibration errors (2 per cent at *C*-band) used as standard by BRATS. While the oldest detected region in each source gives an indication of the age of that population of particles since injection at the hotspot, we do not have a true magnetic field estimate and hence the spectral ages listed in Table 7 are only based on the assumed field strengths. In Section 3.3, we use an analytic model to determine the field strength constrained by our limits, which we then use to re-calculate the spectral ages with our fitted break frequencies.

3.3 Analytic modelling

In this section, we describe the use of an analytic model to simulate the evolution of the lobes of 3C 320 and 3C 444, with the aim of
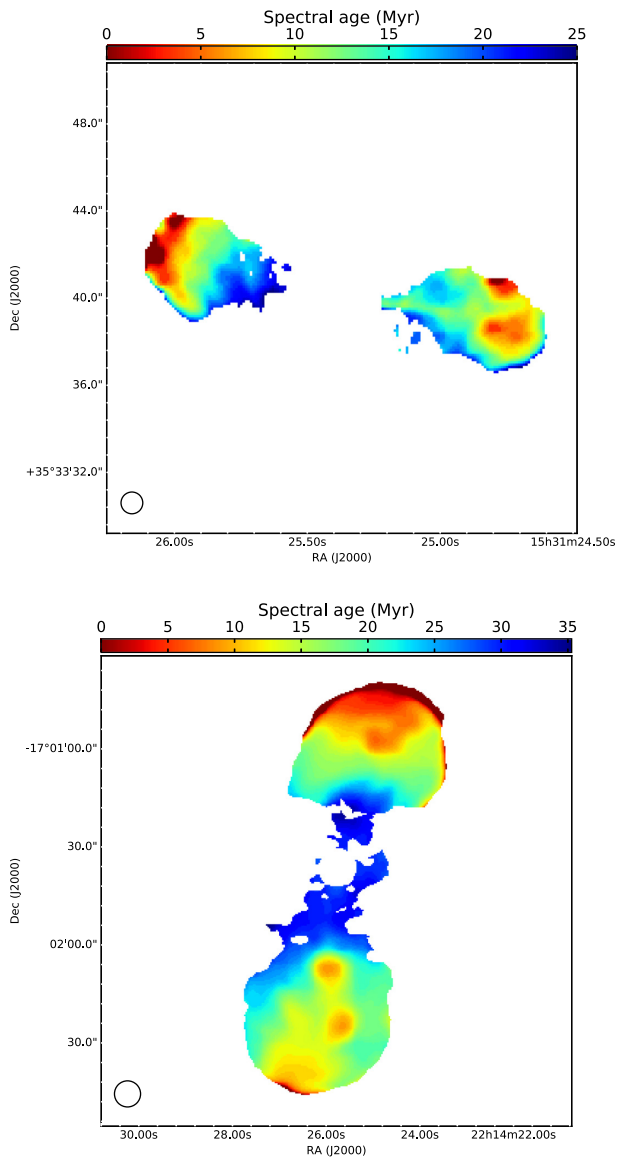
Figure 7. Spectral ageing maps produced by BRATS of 3C 320 (top) and 3C 444 (bottom). The colour wedge shows the ages corresponding to the colour scale. Beam sizes of 0.5 arcsec (top) and 2.0 arcsec (bottom) are shown on the lower left corner. Input injection indices are 0.6 (top) and 0.65 (bottom), while the input lobe magnetic field strengths for these maps are 1 nT (top) and 0.74 nT (bottom). The maximum spectral ages for 3C 320 and 3C 444 in these fits are 25.10 and 30.10 Myr, respectively (see Table 7).

determining more robust source dynamics than would be implied by instantaneous X-ray surface brightness. This will lead to robust source dynamical ages, for comparison with our spectral ages.

We use an analytic model (hereafter the analytic model; Hardcastle 2018), which models the evolution of a 'shocked shell' that is driven by a radio lobe in a particular environment for a particular set of radio source properties [see Hardcastle (2018) for further details of model setup, input, and output parameters]. The modelled dynamics of the shocked shell can be used to approximate the physical properties of the expanding lobes as a function of its dynamical age. We use this model to compute the predicted evolution of shocked shells based on the observed properties of 3C 320 and 3C 444, and then compare their instantaneous measured radio lobe and shock properties against the model predicted properties as a function of

the source age, leading to model dynamical ages constrained by our observations. Using the model lobe magnetic field at the dynamical ages and our fitted break frequencies from Section 3.2, we may determine robust spectral ages and test them against the modelled dynamical ages, where the dynamical evolution is governed by physically realistic environmental information based on our X-ray observations. The usefulness of this particular analytic model has already been tested by its application to a large sample of RLAGN (Hardcastle et al. 2019).

3.3.1 Model setup

In terms of the radio source properties, the model requires; the value of the low-frequency injection index (α_{inj}), the source redshift (z), the ratio of energy density stored in the magnetic field to that in the radiating particles (ζ), and the jet power Q_{jet}. We set α_{inj} equal to the values fitted by BRATS in Section 3.2, which are close to theoretically predicted value based on particle acceleration in radio galaxies (Longair, Ryle & Scheuer 1973). ζ can only be within the range 0–1 – although we can constrain the electron energy density using our radio observations, we do not have an exact value for the magnetic field strength. After running initial test models, the parameter space constrained by our observations resulted in models with ζ only in the range 0–0.5 for 3C 320 and 0–0.1 for 3C 444. Hence, we employ the model for a range of fifty ζ values with equal intervals in the range 0–0.5 and 0–0.1 for 3C 320 and 3C 444, respectively. Similarly for the unknown jet power, for each value of ζ modelled, we ran the model for a range of fifty jet powers in the physically plausible range of $10^{37} \leq Q_{\text{jet}} \leq 10^{39}$ W. We also ran each model for various source inclination angles ($\theta°$) with respect to the observer, with twenty values from $45° \leq \theta \leq 90°$, with $90°$ being a face-on radio galaxy.

In terms of the input environmental properties, the model requires parameters based on either an isothermal beta model, or a universal pressure profile (Arnaud et al. 2010). Throughout our modelling we use an isothermal beta model, as has been used traditionally for many years on observations of X-ray-bright clusters (e.g. Mohr, Mathiesen & Evrard 1999). For a beta model atmosphere the analytic model requires: the beta index β, central density n_0, isothermal temperature kT, central pressure p_0, and the core radius r_c. We obtained the value of these parameters, as described earlier in Section 3.1.2, as estimates of the thermodynamical pre-shocked state of the ICM surrounding 3C 320 and 3C 444. The values of the model input parameters are given in Table 8. 50 000 models were run, for a range of ζ, Q_{jet}, θ, each in a fixed environment. The models were run for a total of 250 time-steps within the range 0.000 01–200 Myr for 3C 320 and 3C 444, with 50 logarithmic steps up to 0.1 Myr, and 200 linear steps thereafter in order to sample well the intermediate and late-stage evolution of the source.

3.3.2 Observationally constrained shell energetics

Example plots of the modelled luminosity–size evolution, for a range of jet powers and a range of inclination angles, at a fixed value of ζ at 0.1 for both sources, are given in Fig. 8. The general lobe luminosity evolution track is as expected from numerical simulations of powerful radio galaxies (Hardcastle & Krause 2013; English et al. 2016): the luminosity starts at a minimum at very early times, then rises to a peak as the total lobe energy increases and the shell expands. The steep fall off at late times, as seen for 3C 320, can be explained as the shell dynamics at this point are governed by

Table 8. Table of input parameters used for the model runs. β is the power-law index for the beta model profile fitted to the environment, kT is the global cluster temperature fitted using an APEC model, p_0 is the central pressure of the ICM using the fitted beta model profile, r_c is the core radius, α_{inj} is the fitted power-law index of the radio source using our spectral ageing analysis (Section 3.2), z is the source redshift, ζ is the ratio of lobe energy densities in magnetic field and electrons, Q_{jet} is the jet power, and θ is the shell inclination angle.

Parameter	3C 320	3C 444
β	$0.67^{+0.04}_{-0.04}$	$0.72^{+0.02}_{-0.02}$
kT (keV)	$2.77^{+2.26}_{-0.85}$	$2.37^{+0.10}_{-0.10}$
p_0 (Pa)	$1.53^{+0.01}_{-0.13} \times 10^{-11}$	$5.09^{+0.07}_{-0.10} \times 10^{-12}$
r_c (kpc)	$82.06^{+5.35}_{-5.94}$	$145.03^{+8.97}_{-8.41}$
α_{inj}	0.6	0.65
z	0.342	0.153
ζ	0–0.5	0–0.1
Q_{jet} (W)	10^{37}–10^{39}	10^{37}–10^{39}
θ ($°$)	45–90	45–90

a much lower environmental density, while radiative and adiabatic expansion losses become more prominent. We also show in Fig. 9, using the same models as in Fig. 8, the lobe magnetic field as a function of lobe size, showing a smooth decrease of the magnetic field strength (in log space) driven by the expansion of the lobes at constant jet power.

We have overplotted dashed lines with shaded regions showing our measured instantaneous lobe 1.5 GHz radio luminosities and physical sizes based on our VLA *L*-band observations (shown in Fig. 1). Flux densities for the luminosity calculation were obtained by drawing a region around the lobes using CASA, and 3σ errors found from the local RMS value, propagated along to find luminosity errors (plotted as grey-shaded regions in Fig. 8 but too narrow to be seen in log space). Physical sizes are based on the largest angular size between the core and hotspot of the lobe showing the clearest hotspot, converted to a physical size using their redshifts. The choice of lobe does not affect the results we present here as orientation effects on the measured size are considered in our models by using a range of inclination angles θ. As well as our observational constraints on the model luminosity and size, we also overplot our constraints on the current lobe magnetic field, given by our equipartition and inverse-Compton-based limits (shaded regions in Fig. 9).

Figs 8 and 9 show that there must exist a number of models that may simultaneously produce the instantaneous observed luminosities within their 3σ errors at the current size of the source within the allowed magnetic field range. Since the slope and position of the luminosity–size and magnetic field evolution is altogether degenerate between Q_{jet}, ζ, and θ, there will in fact be a three-dimensional distribution of the model parameters that may all produce the measured radio luminosity at the projected size within the magnetic field limits, highlighting models that are accepted by all our observational constraints simultaneously.

As well as the observational constraints provided by our radio data, we also apply those provided by our X-ray observations of the central shock. The analytic model also computes the thermodynamics of the shocked shell, which can be used to compare the particle densities and temperatures between those of the modelled shocked shell and those that are measured of the shock seen in our X-ray observations. The extraction of physical information
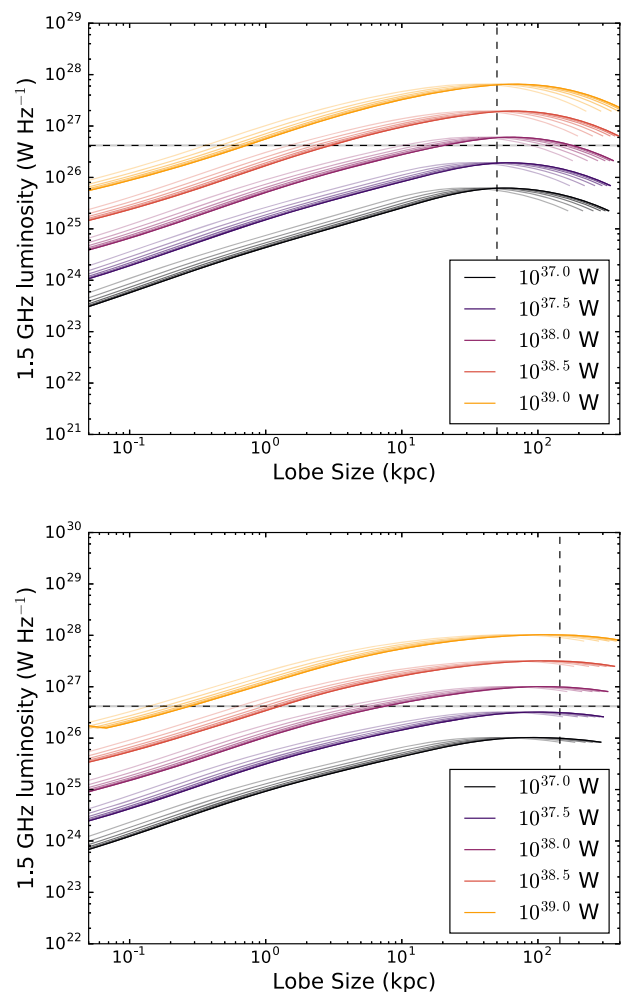
Figure 8. 1.5 GHz radio luminosity evolution for a radio lobe in 3C 320 (upper) and 3C 444 (lower), for a range of plausible jet powers (Q), colour coded as displayed on the legend, for $\zeta = 0.1$. Dashed horizontal and vertical lines indicate the measured properties as given by our VLA 1.5 GHz observations. Grey shaded regions indicate 3σ errors, based on the local RMS level on the radio map. Model lobe sizes with varying source orientation angles are given by transparent lines for each colour: solid lines represent $\theta = 90°$ (edge-on radio galaxy) and the most transparent line for each jet power representing a jet orientation of $\theta = 45°$ with respect to the observer.

from our *Chandra* data for 3C 320 and 3C 444 is explained in Section 3.1.1. Uncertainties on the density measurements were determined by propagation of the 3σ measurement errors from the fitted normalization to the spectra and the uncertainties arising from projection effects on the volume calculations (see Section 3.1.1). Furthermore, for each model run, the volume uncertainties are re-calculated owing to the radio source orientation θ changing the projected lobe size that should be subtracted from the original shock volume calculation. This essentially allows the radio source orientation to vary independently to the orientations considered for the shock, with the orientations of the shock included as fixed upper and lower limits to the volume. The uncertainties, listed in Table 4, allow us to select models that agree with our X-ray-based constraints on the shock.

In Figs 10 and 11, we plot the particle density and temperature of the modelled shocked shell against age (not including the variable uncertainties on the shock volume for each model), for
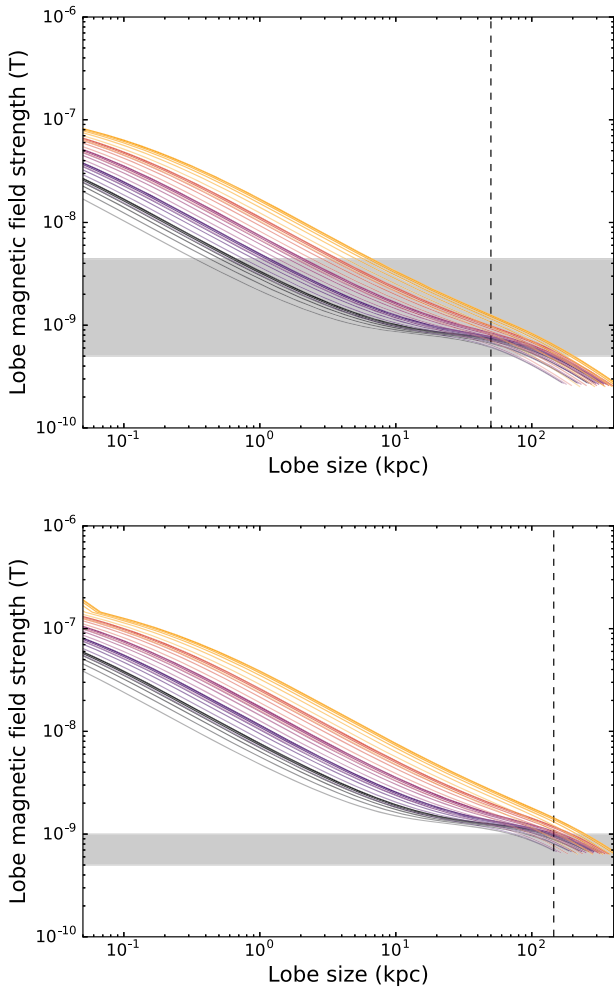
Figure 9. Magnetic field evolution for a radio lobe in 3C 320 (upper) and 3C 444 (lower), for a range of plausible jet powers (Q), colour coded as displayed on the legend (as in Fig. 8). Grey shaded regions indicate our measured upper and lower limit magnetic fields, given by the equipartition assumption and measured inverse-Compton upper limits, respectively. The dashed vertical line and transparent coloured lines are defined as in Fig. 8.

all models that simultaneously agree with our measured luminosity, size, and magnetic field constraints. As can be seen, the shock density and temperatures vary very little between models for the range of model parameters accepted by our observations – this is solely driven by the narrow range of jet powers constrained by our relatively small instantaneous luminosity errors, centred at $\sim 1.5 \times 10^{37}$ W for 3C 320 and $\sim 2.5 \times 10^{37}$ W for 3C 444. We have again overplotted dashed lines and shaded regions showing our instantaneous measured particle densities and temperatures and their errors, respectively, of the shock region from our X-ray observations (see Section 3.1.1). We may then use both our radio and X-ray-based observational constraints to highlight those models in the three-dimensional $Q - \zeta - \theta$ parameter space that are 'accepted' by our measured instantaneous physical properties of the sources. Figs 12 and 13 display these distributions for 3C 320 and 3C 444, respectively. Light grey points show all model runs, cyan points show models constrained by our X-ray shock observations, and black points show models constrained by our radio observations. Red points, crucially, show the models constrained
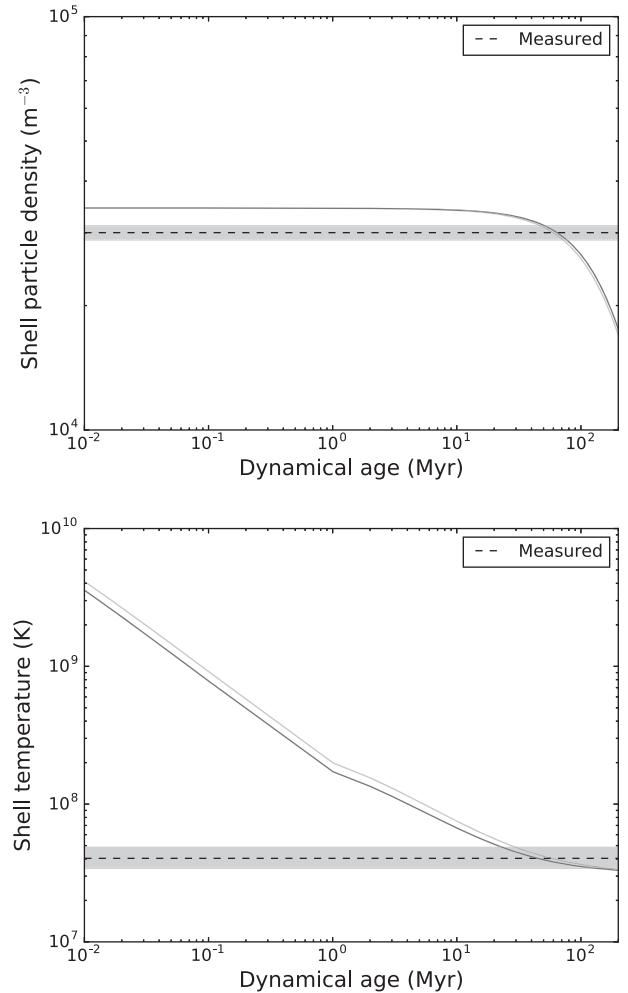
Figure 10. Shell electron density and temperature against the source age for 3C 320, for all accepted model runs (red points in Fig. 12). Dashed lines and grey shaded regions show our instantaneous measured values and 3σ errors from our X-ray observations, respectively.

by both our radio and X-ray observations simultaneously. For both sources, a similar shape in distribution of accepted models is seen, with particularly narrow ranges in jet power – as can be seen in Fig. 8 our luminosity measurement errors, by which different jet powers can be constrained, are fairly small compared to our uncertainties on other parameters (i.e B-field, density, temperature). For 3C 320 we see a larger range in values of ζ, owing to the looser constraints on the lobe magnetic field (0.5–4.4 nT) than for 3C 444 (0.5–1.0 nT). Most source orientation angles θ are permitted, as expected, as we do not have fixed constraints on the true orientation angles to the plane of the sky. Interestingly, we see that the combination of radio and X-ray data for the radio source and the shock, respectively, constrain a particular set of model parameters that are more tightly constrained than the separate constraints from the data (compare red points to the black and cyan).

3.3.3 Model dynamical and spectral ages

For each model run, the shocked shell properties are calculated from which the lobe properties are inferred, at each time-step, or, at each dynamical age between 0 and 200 Myr. At the time where the model
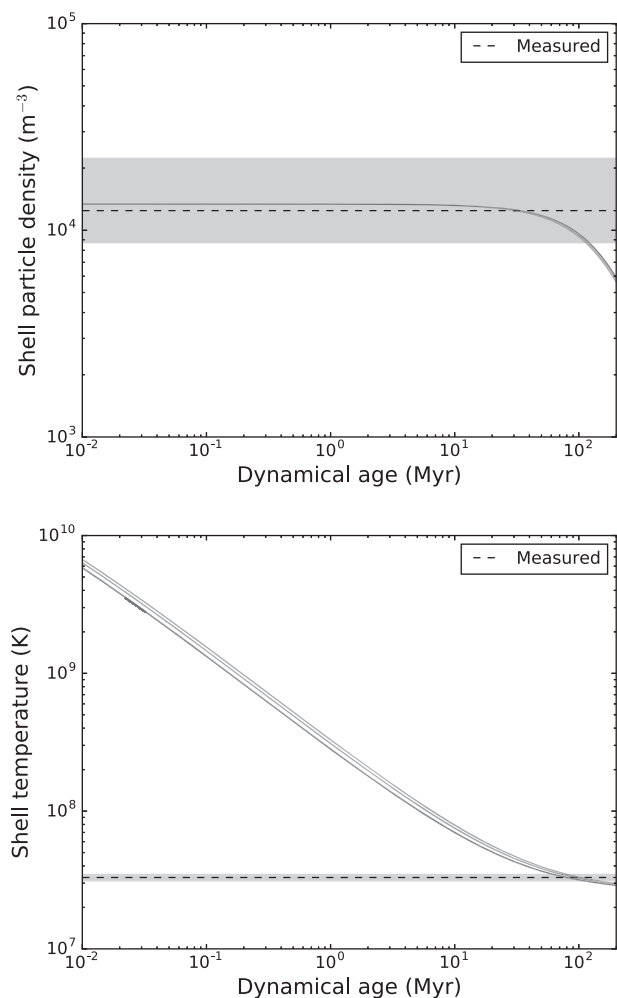
Figure 11. Shell electron density and temperature against the source age for 3C 444, for all accepted model runs (red points in Fig. 13). Dashed lines and grey shaded regions show our instantaneous measured values and 3σ errors from our X-ray observations, respectively.

properties agree with our instantaneously measured properties and their limits (red points), we compare each model dynamical age with an estimate of the spectral age of the source. As mentioned previously the crude spectral ages obtained in Section 3.2 cannot directly be used as comparison since the true magnetic field was unknown. Instead, we use the magnetic field at the dynamical age of the source from our accepted models to re-compute spectral ages. Rather than employing BRATS to re-compute spectral ages for each model magnetic field, as would be computationally and time-expensive, we simply use equation (1) for the spectral age, using the break frequency ν_b which has been obtained from the Tribble model fits in Section 3.2, and the magnetic field B for each model. Thus, for each accepted model (red and black points in Figs 12 and 13), we obtain a model dynamical age and a spectral age based on a magnetic field associated with that model, with models being consistent with our radio and X-ray observations.

In Fig. 14, we plot the distributions of the dynamical age/spectral age ratio (t_{dyn}/t_{spec}) for all accepted models (grey) and models accepted by both radio and X-ray constraints (red), for 3C 320 and 3C 444. Most of the models have a large age discrepancy, with a large fraction of models having $t_{dyn}/t_{spec} > 2$. It is interesting to see

that for 3C 444, the models constrained by both radio and X-ray data return the best agreement between spectral and dynamical ages. This highlights the importance of obtaining accurate information on the source physical properties to obtain spectral ages, and in particular, the magnetic field strength. In Fig. 15, we plot t_{dyn}/t_{spec} against the lobe magnetic field for the accepted models (those that satisfy our radio-based constraints in transparent colours, and those that satisfy both radio and X-ray observations in opaque colours). We colour code each point by their value of ζ, to provide a reference for each magnetic field to its value relative to equipartition ($\zeta = 1$ gives an equal distribution of energy towards the magnetic field and radiating particles). It can be clearly seen that the dynamical age/spectral age discrepancy increases as ζ increases, i.e as ζ goes to 1 (equipartition) the lobe magnetic field systematically gives a spectral age that disagrees more with the dynamical age, as predicted by Harwood et al. (2016) (hereafter H16). Spectral ages from equipartition magnetic fields are underestimated. This is consistent with inverse-Compton-based magnetic field estimates, where the population of RLAGN show a departure from equipartition (Croston et al. 2004, 2005; Ineson et al. 2017) – the latter study finding a median in the distribution of all sources at $B = 0.4B_{eq}$. The spectral ages with the smallest discrepancy with their dynamical ages for 3C 320 and 3C 444 are 25 and 42 Myr, respectively.

Our results, combined with those from other previously mentioned studies (Section 1.3.3), suggest that the lobes of radio galaxies are not at equipartition. The total energy injected by the jets distributes more energy to the radiating particles in the lobes than the magnetic fields, than would be assumed by minimizing the total energy in the lobes. As can be seen in Fig. 15, our observations require that $B_{lobe} \leq 0.1B_{eq}$ for 3C 320 and $B_{lobe} \leq 0.5B_{eq}$ for 3C 444, for the best agreement between the dynamical and spectral ages. Interestingly, a lobe magnetic field that maximizes the spectral age (differentiating equation 1 with respect to B) gives $B = B_{CMB}/\sqrt{3}$, indeed gives $B_{lobe} \approx 0.1B_{eq}$ for 3C 320 and $B_{lobe} \approx 0.2B_{eq}$ for 3C 444. Shelton, Hardcastle & Croston (2011) find $B = 0.3B_{eq}$ for the FR-II source 3C 452, a similarly powerful source in a hot intragroup medium, which may suggest similar departure levels from equipartition for sources in rich environments, though we cannot state this with any significance since there are few powerful FR-IIs in cluster environments at low redshift. These and other similar departures from equipartition are discussed further in the next section.

We overplot dashed lines at a discrepancy factor of two in Fig. 15 to highlight that the discrepancy may be due to electron mixing – Turner et al. (2017) show, using numerical hydrodynamical simulations of radio galaxies with radiative losses, that the spectral and dynamical age can be discrepant by a factor of a few, or two at minimum, due to the fact that different populations of electrons mix in the lobes due to turbulent flows, particularly towards the base of the lobes. Even near the core region, where the oldest electrons exist, the observed spectrum can be dominated by younger electrons due to mixing, increasing the observed break frequency, and decreasing the modelled spectral age relative to the true age. The Tribble and JP models of spectral ageing used in this study do not take into account this physical process, as they assume that all the electrons contributing to the model spectrum at any point all have similar ages. The magnitude of mixing that occurs for any particular source cannot currently be measured from observations, nor can it be inferred for a population of sources. Even well-resolved spectral studies are limited by this mixing factor, which can only be traced by numerical simulations. We suggest that, in the application of resolved ageing models to broad-band data,
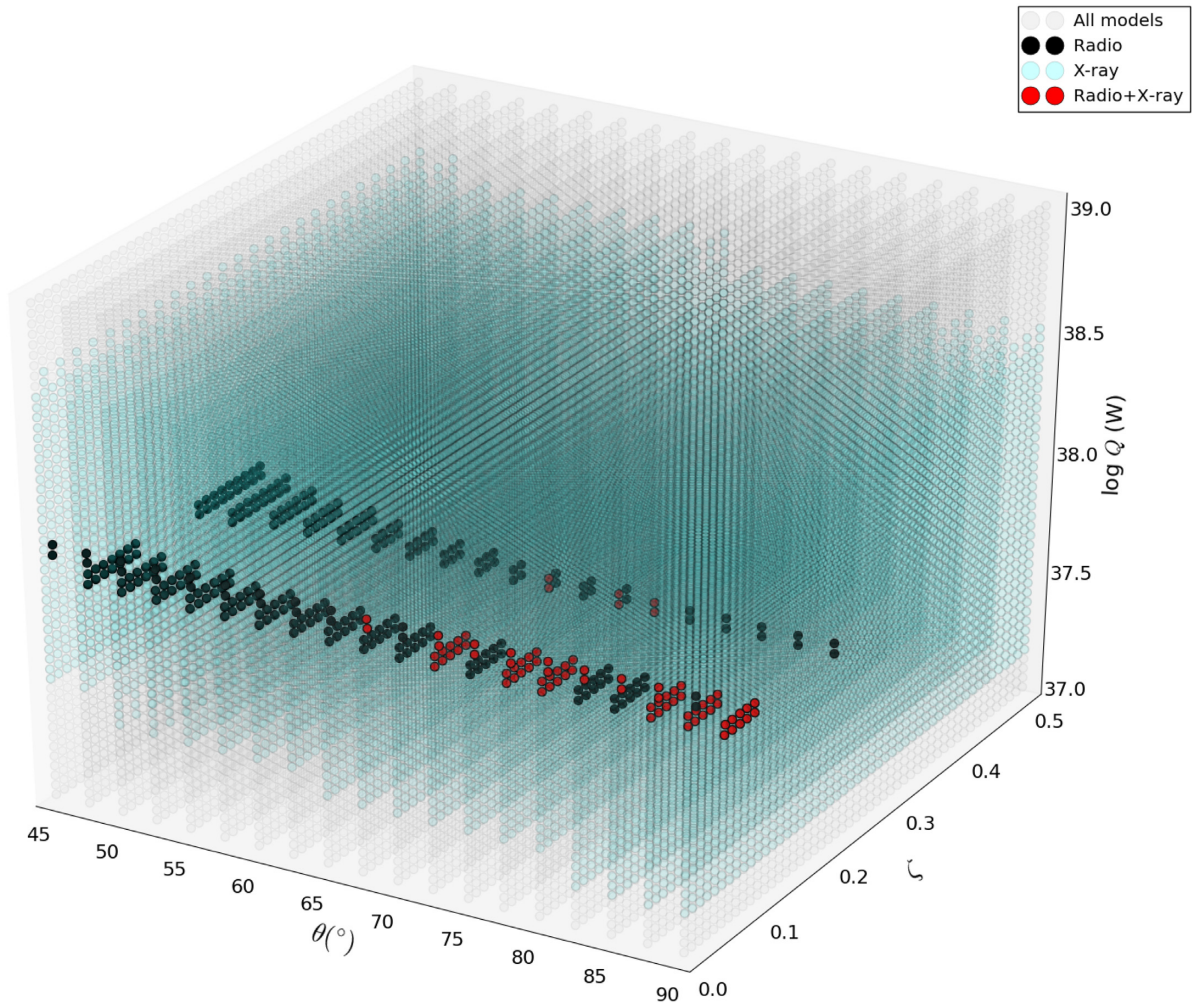
Figure 12. Three-dimensional grid displaying all model runs for 3C 320 for each jet power (Q_{jet}), ζ, and θ (grey points). Cyan points highlight the models reproducing our X-ray shock density and temperature measurements, black points highlight models reproducing the 1.5 GHz radio luminosity, lobe magnetic field and projected physical size constraints, and red models are those that match both radio and X-ray constraints.

the spectral age/dynamical age discrepancy can be significantly reduced by using a correct estimate of the magnetic field strength, and a scaling factor of $\sim$2 at minimum to account for electron mixing.

This scaling factor, however, is strongly dependent on the lobe magnetic field strength used for the spectral age calculation. The magnetic field strengths output at each dynamical age in our dynamical models are the current field strengths in the lobes at that age, as would be measured observationally as an instantaneous measurement, rather than an *effective* field strength that takes into account the time-evolution of the magnetic field experienced by the same particles throughout the source lifetime. The effective magnetic field would be larger at any given time relative to the current field strength, making spectral ages younger and hence more discrepant with dynamical ages. Running the models using an effective time-integrated magnetic field, as can be output by the analytic model, we find that for a source at an age ≥ 1 Myr, the effective magnetic field strength is a factor $\sim$2 greater than the current magnetic field strength at each age. This leads to a larger discrepancy between spectral and dynamical ages by a factor $\sim$2, for each of the models shown in Figs 14 and 15. The currently existing ageing models (i.e JP, Tribble) cannot determine effective

field strengths for fixed electron populations while fitting for the age itself, and better models are needed to incorporate effective magnetic fields for differently aged populations. The use of the current lobe magnetic field at any dynamical age does not affect the main conclusions of this paper.

4 DISCUSSION

In this section, we discuss our results in probing the spectral age/dynamical age problem, and their implications on determining spectral ages of the population of radio galaxies in upcoming large-area radio surveys.

4.1 Can we trust spectral ages?

For 3C 320 and 3C 444, we have found that the spectral and dynamical age discrepancy still exists, but decreases the lower the magnetic field – for the spectral age modelled using the Tribble model, the spectral and dynamical ages can *only* be reconciled based on a relatively large departure from the equipartition magnetic field strength ($B \approx 0.1 B_{\mathrm{eq}}$ and $B \approx 0.5 B_{\mathrm{eq}}$) for 3C 320 and 3C 444,
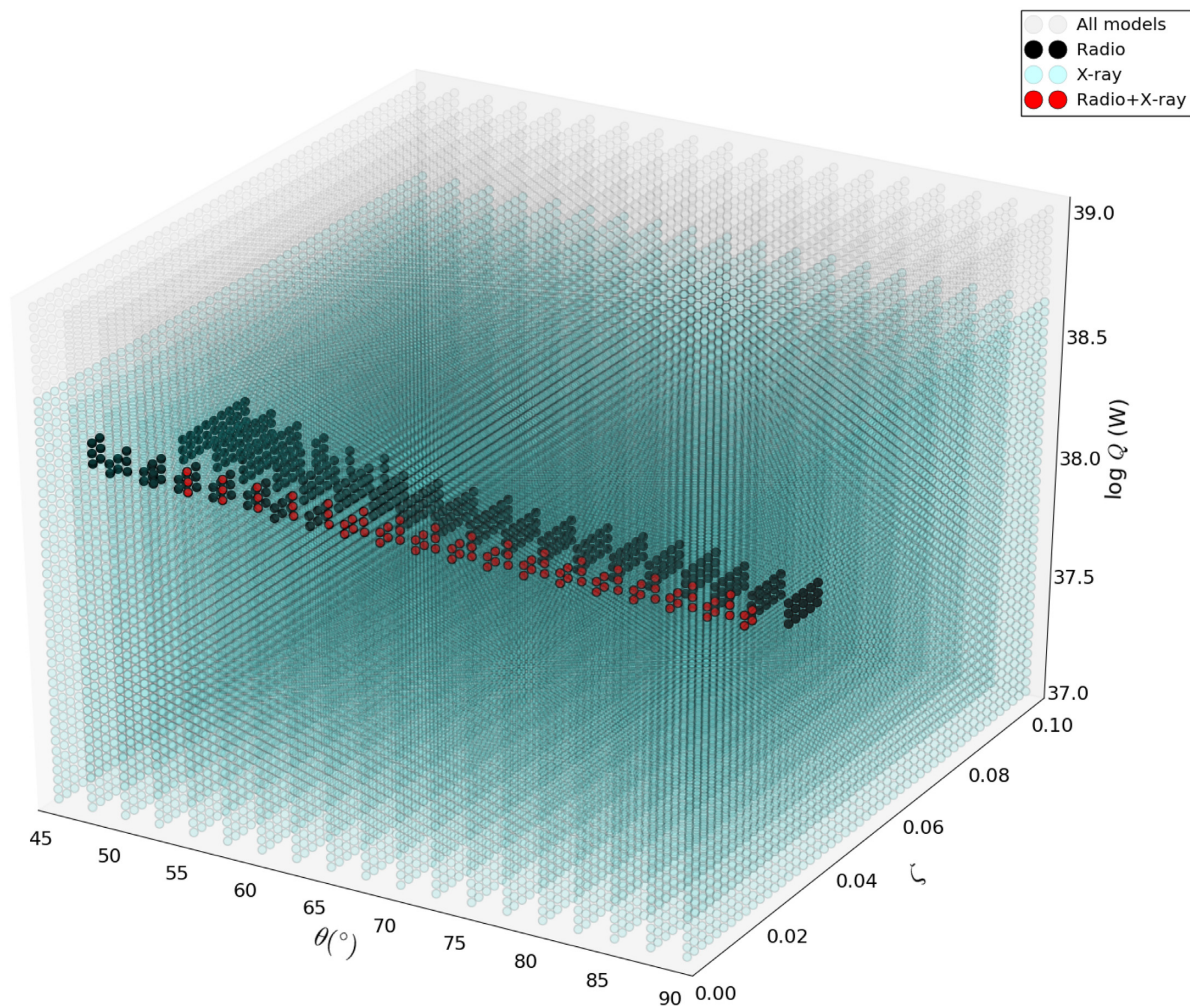
Figure 13. Three-dimensional grid displaying all model runs for 3C 444 for each jet power (Q_{jet}), ζ, and θ (grey points). Cyan points highlight the models reproducing our X-ray shock density and temperature measurements, black points highlight models reproducing the 1.5 GHz radio luminosity, lobe magnetic field and projected physical size constraints, and red models are those that match both radio and X-ray constraints.

respectively. That is, a magnetic field near the inverse-Compton-based lower limits gives the best agreement for both sources (down to a factor of 2). The corresponding ratio of the lobe magnetic field to that at equipartition for 3C 320 is generally lower than that estimated for other samples of FR-II radio galaxies (Hardcastle et al. 1998, 2002), particularly lower than the minimum found in more recent studies (Croston et al. 2005; Ineson et al. 2017). Reconciling with the work from H13, a maximum spectral age occurs when $B = B_{\text{CMB}}/\sqrt{3}$, leading to a field strength of $B = 0.25B_{\text{eq}}$ for 3C 436. This is also a large departure from their assumed equipartition field strengths, and would drive their spectral ages into more of an agreement to their older derived dynamical age for this source. This may suggest a common departure of $B \approx 0.1B_{\text{eq}} - 0.5B_{\text{eq}}$ for powerful radio galaxies in clusters. This is not physically unrealistic since there is no a priori reason to believe that equipartition fields are the true field strengths in the lobes of radio galaxies, other than that they are close to the field strengths for which the total energy content in the lobes is minimized.

A major caveat in the use of observations to determine spectral ages is that the faintest detectable synchrotron emission in a given observation does not necessarily relate to the oldest population of particles. It is possible that emission from significantly older popu-

lations that have been radiating for a long period of time is below the sensitivity limits of our VLA observations. Particularly for 3C 320, as seen in Fig. 1 or in Fig. 7, the most aged emission near the core is clearly not detected at *C* band. Higher sensitivity is required in order to capture the oldest populations which are located towards the radio core. For 3C 320, we tried including all of the highest frequency bandwidth *C*-band maps (which were originally removed from the analysis as they contained less detectable emission from the oldest regions near the core) but this resulted in a decrease of the maximum spectral age only by $\sim$1 Myr. While the results of this paper are unchanged by not including the highest frequency maps, older undetected emission might still be present. The addition of sensitive observations at even lower frequencies than those presented in this study, such as those that can be provided by the Low Frequency Array (LOFAR; van Haarlem et al. 2013), will allow the detection of fainter emission that is crucial to spectral ageing studies (e.g. H16, H17).

We emphasize that these results only apply to large and powerful FR-II sources for which lobe particle contents are well understood. The lobe energetics for FR-I sources cannot be modelled in the same way and are less well understood. Equipartition assumptions for FR-Is tend to lead to an apparent lobe underpressure with respect
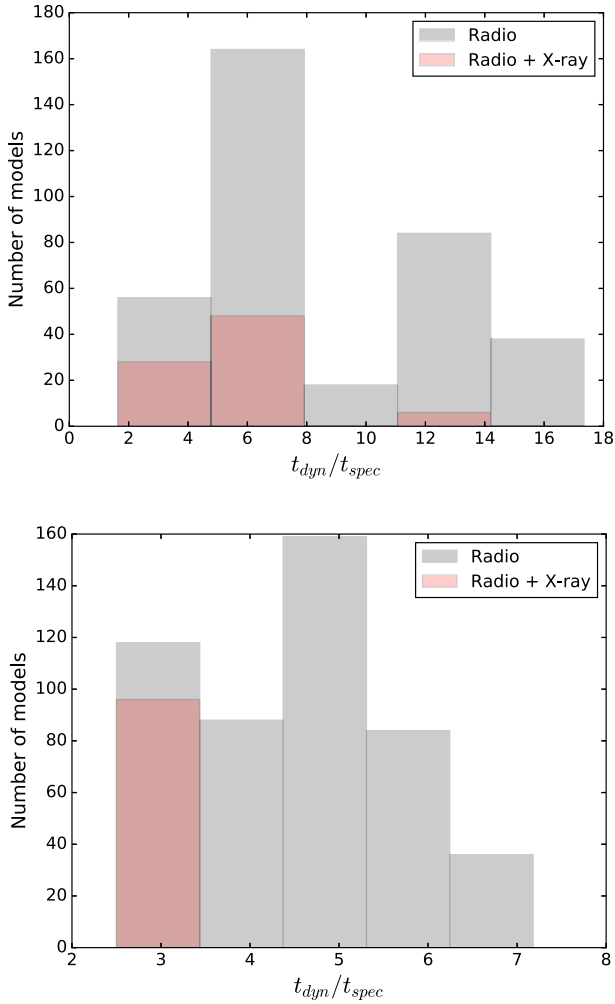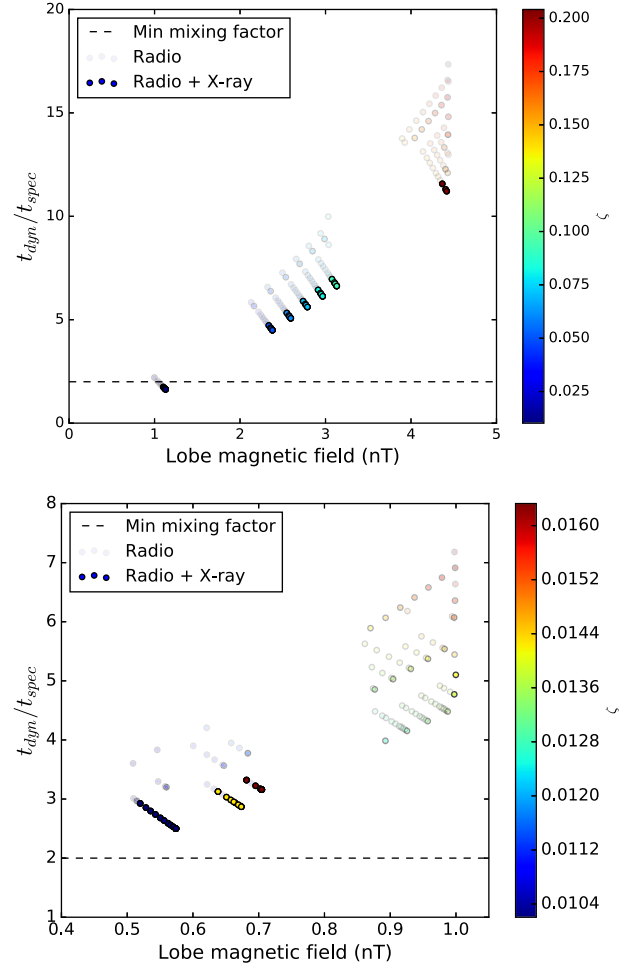
Figure 14. Distribution of the ratio of the dynamical age to the spectral age, for our observationally permitted models for 3C 320 (top) and 3C 444 (bottom).

Figure 15. Lobe magnetic field against the dynamical age/spectral age discrepancy for 3C 320 (top) and 3C 444 (bottom), for all accepted model runs (red points in Figs 12 and 13). Points have been colour coded by their value of ζ. The horizontal dashed line has been drawn at an age ratio of two – the minimum effect of electron mixing according to numerical models (Turner et al. 2017).

to their external medium and they are therefore thought to contain a significant fraction of massive particles (Croston et al. 2008; Croston, Ineson & Hardcastle 2018).

4.2 Injection index

For spectral ageing studies, the slope of the low-frequency power-law spectrum was traditionally assumed to take on values around ~0.5–0.7 (e.g. Carilli et al. 1991). More recent studies by H13 and H15, without broad-band low-frequency data, tested these assumptions using BRATS and found much steeper injection indices at ~0.80–0.85. One might expect that the addition of low-frequency data constraining the power-law gradient would yield flatter injection indices – our broad-band data at 1.4 GHz for 3C 320 and 3C 444 give best-fitting injection indices of ~0.60–0.65, closer to the traditionally expected values. However, even with the inclusion of MHz-frequency data, H16, H17 still find $0.7 \leq \alpha_{inj} \leq 0.85$. Variations in instrument capabilities aside (i.e broad-band versus narrow-band spectra), a range in α_{inj} is routinely found in FR-II radio galaxies, but it is interesting to discuss the physical source properties that may lead to particular observed

values of α_{inj}, particularly since steeper injection indices that cause younger spectral ages to be derived may cause a discrepancy with dynamical ages. 3C 320 and 3C 444 are, along with Cygnus A, a group of only a handful of powerful FR-II sources that are found in rich cluster environments. These sources are found to have injection indices of $\alpha_{inj} \leq 0.65$ (Carilli et al. 1991 find $\alpha_{inj} \sim 0.5$ for Cygnus A), while interestingly, the FR-II sources in sparser environments studied by H13, H15, H16, H17 have $\alpha_{inj} \geq 0.7$. The large-scale environment may play a role in determining the injection index we observe – an obvious argument for this being that FR-II sources in much denser environments would require a higher jet power to drive through the surrounding medium than those in sparser environments, thereby driving stronger Fermi acceleration at the terminal shock. Indeed, jet power is known to be strongly correlated with injection index (Konar & Hardcastle 2013) which supports this scenario. As mentioned, particularly with small-sample statistics, systematic effects arising from the measurement of injection indices must be borne in mind, and larger samples of FR-II sources with broad-band data are required to test any relationship between environment and injection index.

4.3 Jet powers

Our self-consistent dynamical models have constrained narrow ranges of jet powers that are permitted by our radio source and X-ray ICM observations (red points in Figs 12 and 13). For these models we find $5.96 \times 10^{37}\,\mathrm{W} \leq Q_{\mathrm{jet},\,3C320} \leq 1.05 \times 10^{38}\,\mathrm{W}$, and $1.53 \times 10^{38}\,\mathrm{W} \leq Q_{\mathrm{jet},\,3C444} \leq 2.22 \times 10^{38}\,\mathrm{W}$. For the models with the minimum discrepancy between spectral and dynamical ages, we have $Q_{\mathrm{jet},\,3C320} = 1.05 \times 10^{38}\,\mathrm{W}$ and $Q_{\mathrm{jet},\,3C444} = 2.22 \times 10^{38}$ W. These are generally higher than the cavity power measurements, via a cavity buoyancy time-scale, made by Vagshette et al. (2019, $P_{\mathrm{cav},\,3C\,320} = 3.52^{+6.75}_{-1.85} \times 10^{37}$) and Vagshette et al. (2017, $P_{\mathrm{cav},\,3C\,444} = 6.13^{+18.84}_{-2.34} \times 10^{37}$), though the latter measurement has large uncertainties and our jet power for 3C 444 is close to their upper limit. As stated in Section 1.3.3 such instantaneous measurements are unreliable, and in this case they lead to an underestimation of the jet power, as shown by comparison to our more robust calculations. The cooling luminosity of the cluster emission surrounding 3C 320 and 3C 444 up to 100 kpc from the centre was found by Vagshette et al. (2017, 2019) to be $L_{\mathrm{cool},3C\,320} = 8.48^{+0.15}_{-0.28} \times 10^{37}$ W and $L_{\mathrm{cool},3C\,444} = 8.30^{+0.02}_{-0.20} \times 10^{37}$ W, respectively, suggesting that the mechanical powers delivered by the jets are sufficient to balance and overcome the radiative losses in the ICM.

5 CONCLUSIONS

In order to develop the kinetic jet luminosity function (the number density of RLAGN at each jet power), an accurate and reliable age is required. Given that the ages are accurately derived, and therefore the jet power, we can then essentially derive kinetic powers for all (FR-II) RLAGN out to high redshifts. This will in fact become possible in the near future with the large numbers of radio galaxies that will be observed in large area radio surveys, which will have the resolution and sensitivity to produce high fidelity images of radio galaxies out to high redshift where powerful FR-IIs are more common. As a tool to determine source ages, the use of spectral ageing in the population of FR-II sources is crucial, and does not require deep X-ray observations.

In this work, with sensitive, broad-band and high-resolution observations, coupled with the use of an analytic model to determine robust dynamical ages, we have probed the dynamical age/spectral age problem.

(i) We have used analytic-based dynamical models to constrain a particular set of jet powers, magnetic fields, spectral ages, and dynamical ages that are self-consistent and agree with our radio observations of the radio galaxies 3C 320 and 3C 444, and their surrounding shocked gas as observed in X-rays.

(ii) The spectral ages which give the least discrepancy with respect to observationally constrained modelled dynamical ages are ∼25 and ∼42 Myr for 3C 320 and 3C 444, respectively. The minimum discrepancy factors are ∼2 and ∼2.5, respectively.

(iii) The dynamical age/spectral age discrepancy increases with the assumption of an equipartition field strength in our models. Hence, the magnetic field strength must be directly measured using inverse-Compton measurements or inferred using a suitable departure from equipartition to determine accurate age estimates.

(iv) Particle mixing by differently aged populations, as is thought to occur physically due to turbulence, leads to a factor of a few discrepancy in the dynamical age/spectral age problem, as numerically calculated by Turner et al. (2017). Hence, the combination of a correct field estimate and a multiplicative factor of at least two to

the spectral age will remove significant discrepancies relative to the source dynamical age.

(v) When using resolved spectral ageing models, broadbandwidth data that sample the power law and spectral curvature due to ageing are crucial for determining accurate spectral ages. We find that the low-frequency injection indices for our rich-cluster sources are flatter ($\alpha_{\mathrm{inj}} \sim 0.6$) than those found in recent similar work for sources in sparser environments (H13, H15, H16, H17), suggesting that the environment may be linked to the observed injection index for powerful FR-II sources.

(vi) Jet powers based on *pdV* estimates of cavities or instantaneous shock measurements and source ages based on buoyancy time-scales are incorrect, and lead to underestimates of the kinetic feedback of radio galaxies – we suggest that analytic or numerical models constrained by observations are better in robustly determining the energetics and dynamics of radio galaxies.

REFERENCES

Alexander P., 1987, MNRAS, 225, 27
Alexander P., Leahy J. P., 1987, MNRAS, 225, 1
Arnaud M., Pratt G. W., Piffaretti R., Böhringer H., Croston J. H., Pointecouteau E., 2010, A&A, 517, A92
Bell A. R., 1978, MNRAS, 182, 147
Best P. N., 2004, MNRAS, 351, 70
Best P. N., Heckman T. M., 2012, MNRAS, 421, 1569
Bîrzan L., Rafferty D. A., McNamara B. R., Wise M. W., Nulsen P. E. J., 2004, ApJ, 607, 800
Bîrzan L., McNamara B. R., Nulsen P. E. J., Carilli C. L., Wise M. W., 2008, ApJ, 686, 859
Brienza M., et al., 2016, A&A, 585, A29

Brienza M., et al., 2017, A&A, 606, A98

Carilli C. L., Perley R. A., Dreher J. W., Leahy J. P., 1991, ApJ, 383, 554

Cavagnolo K. W., McNamara B. R., Nulsen P. E. J., Carilli C. L., Jones C., Bîrzan L., 2010, ApJ, 720, 1066

Cavaliere A., Fusco-Femiano R., 1978, A&A, 70, 677

Croston J. H., Birkinshaw M., Hardcastle M. J., Worrall D. M., 2004, MNRAS, 353, 879

Croston J. H., Hardcastle M. J., Harris D. E., Belsole E., Birkinshaw M., Worrall D. M., 2005, ApJ, 626, 733

Croston J. H., Kraft R. P., Hardcastle M. J., 2007, ApJ, 660, 191

Croston J. H., Hardcastle M. J., Birkinshaw M., Worrall D. M., Laing R. A., 2008, MNRAS, 386, 1709

Croston J. H., et al., 2009, MNRAS, 395, 1999

Croston J. H., Hardcastle M. J., Mingo B., Evans D. A., Dicken D., Morganti R., Tadhunter C. N., 2011, ApJ, 734, L28

Croston J. H., Ineson J., Hardcastle M. J., 2018, MNRAS, 476, 1614

Croton D. J., et al., 2006, MNRAS, 365, 11

Dabhade P., Gaikwad M., Bagchi J., Pandey-Pommier M., Sankhyayan S., Raychaudhury S., 2017, MNRAS, 469, 2886

Eilek J. A., 1996, in Hardee P. E., Bridle A. H., Zensus J. A., eds, ASP Conf. Ser. Vol. 100, Energy Transport in Radio Galaxies and Quasars. Astron. Soc. Pac., San Francisco, p. 281

English W., Hardcastle M. J., Krause M. G. H., 2016, MNRAS, 461, 2025

Erlund M. C., Fabian A. C., Blundell K. M., Celotti A., Crawford C. S., 2006, MNRAS, 371, 29

Fanaroff B. L., Riley J. M., 1974, MNRAS, 167, 31P

Fruscione A., et al., 2007, Chandra News, 14, 36

Gaspari M., Brighenti F., Temi P., 2012, MNRAS, 424, 190

Godfrey L. E. H., Shabala S. S., 2013, ApJ, 767, 12

Goodger J. L., Hardcastle M. J., Croston J. H., Kassim N. E., Perley R. A., 2008, MNRAS, 386, 337

Hardcastle M. J., 2013, MNRAS, 433, 3364

Hardcastle M. J., 2018, MNRAS, 475, 2768

Hardcastle M. J., Croston J. H., 2010, MNRAS, 404, 2018

Hardcastle M. J., Krause M. G. H., 2013, MNRAS, 430, 174

Hardcastle M. J., Birkinshaw M., Worrall D. M., 1998, MNRAS, 294, 615

Hardcastle M. J., Worrall D. M., Birkinshaw M., Laing R. A., Bridle A. H., 2002, MNRAS, 334, 182

Hardcastle M. J., et al., 2019, A&A, 622, A12

Hargrave P. J., Ryle M., 1974, MNRAS, 166, 305

Harwood J. J., 2017, MNRAS, 466, 2888(H17)

Harwood J. J., Hardcastle M. J., Croston J. H., Goodger J. L., 2013, MNRAS, 435, 3353(H13)

Harwood J. J., Hardcastle M. J., Croston J. H., 2015, MNRAS, 454, 3403(H15)

Harwood J. J., et al., 2016, MNRAS, 458, 4443(H16)

Heesen V., Croston J. H., Harwood J. J., Hardcastle M. J., Hota A., 2014, MNRAS, 439, 1364

Heinz S., Reynolds C. S., Begelman M. C., 1998, ApJ, 501, 126

Heinz S., Brueggen M., Ruszkowski M., Young A., 2007, American Astronomical Society Meeting Abstracts, #125.01

Högbom J. A., 1974, A&AS, 15, 417

Ineson J., Croston J. H., Hardcastle M. J., Kraft R. P., Evans D. A., Jarvis M., 2013, ApJ, 770, 136

Ineson J., Croston J. H., Hardcastle M. J., Mingo B., 2017, MNRAS, 467, 1586

Jaffe W. J., Perola G. C., 1973, A&A, 26, 423

Kaiser C. R., Alexander P., 1997, MNRAS, 286, 215

Kaiser C. R., Schoenmakers A. P., Röttgering H. J. A., 2000, MNRAS, 315, 381

Konar C., Hardcastle M. J., 2013, MNRAS, 436, 1595

Kraft R. P., Vázquez S. E., Forman W. R., Jones C., Murray S. S., Hardcastle M. J., Worrall D. M., Churazov E., 2003, ApJ, 592, 129

Kraft R. P., et al., 2007, ApJ, 665, 1129

Leahy J. P., 1991, Cambridge University Press, Cambdrige Astrophyics Series, No. 19, Interpretation of Large Scale Extragalactic Jets. p. 100

Liu W., et al., 2019, MNRAS, 484, 3376

Lobanov A. P., 1998, A&A, 330, 79

Longair M. S., 2011, High Energy Astrophysics, Cambridge University Press 2011, 3rd edition, Cambridge University Press

Longair M. S., Ryle M., Scheuer P. A. G., 1973, MNRAS, 164, 243

Mahatma V. H., 2017, Master's thesis, Univ. Hertfordshire

Mahatma V. H., et al., 2018, MNRAS, 475, 4557

Mandel E., Murray S. S., Roll J. B., 2001, in Harnden F. R., Jr, Primini F. A., Payne H. E., eds, ASP Conf. Ser. Vol. 238, Astronomical Data Analysis Software and Systems X. Astron. Soc. Pac., San Francisco, p. 225

Massaro F., Harris D. E., Tremblay G. R., Liuzzo E., Bonafede A., Paggi A., 2013, ApJS, 206, 7

Meisenheimer K., Roser H.-J., Hiltner P. R., Yates M. G., Longair M. S., Chini R., Perley R. A., 1989, A&A, 219, 63

Mingo B., Hardcastle M. J., Croston J. H., Dicken D., Evans D. A., Morganti R., Tadhunter C., 2014, MNRAS, 440, 269

Mohr J. J., Mathiesen B., Evrard A. E., 1999, ApJ, 517, 627

Morganti R., Killeen N. E. B., Tadhunter C. N., 1993, MNRAS, 263, 1023

O'Sullivan E., Giacintucci S., David L. P., Gitti M., Vrtilek J. M., Raychaudhury S., Ponman T. J., 2011, ApJ, 735, 11

Offringa A. R., van de Gronde J. J., Roerdink J. B. T. M., 2012, A&A, 539, A95

Perley R. A., Butler B. J., 2013, ApJS, 204, 19

Rafferty D. A., McNamara B. R., Nulsen P. E. J., Wise M. W., 2006, ApJ, 652, 216

Ramos Almeida C., Tadhunter C. N., Inskip K. J., Morganti R., Holt J., Dicken D., 2011, MNRAS, 410, 1550

Sabater J., et al., 2019, A&A, 622, A17

Scheuer P. A. G., 1974, MNRAS, 166, 513

Shelton D. L., Hardcastle M. J., Croston J. H., 2011, MNRAS, 418, 811

Shulevski A., Morganti R., Oosterloo T., Struve C., 2012, A&A, 545, A91

Tribble P. C., 1993, MNRAS, 261, 57

Turner R. J., 2018, MNRAS, 476, 2522

Turner R. J., Shabala S. S., 2015, ApJ, 806, 59

Turner R. J., Rogers J. G., Shabala S. S., Krause M. G. H., 2017, MNRAS, 473, 4179

Vagshette N. D., Naik S., Patil M. K., Sonkamble S. S., 2017, MNRAS, 466, 2054

Vagshette N. D., Naik S., Patil M. K., 2019, MNRAS, 485, 1981

van Haarlem M. P., et al., 2013, A&A, 556, A2

Wylezalek D., Zakamska N. L., 2016, MNRAS, 461, 3724

This paper has been typeset from a TEX/LATEX file prepared by the author.